

1 **Competition between water uptake and ice nucleation by**
2 **glassy organic aerosol particles**

3

4 **T. Berkemeier^{1,2}, M. Shiraiwa¹, U. Pöschl¹ and T. Koop^{2,*}**

5 [1] Multiphase Chemistry Department, Max Planck Institute for Chemistry, Mainz, Germany

6 [2] Faculty of Chemistry, Bielefeld University, Bielefeld, Germany

7

8 Correspondence to: T. Koop (thomas.koop@uni-bielefeld.de)

9

10 *To be submitted to Atmospheric Chemistry and Physics (ACP)*

11

12 Short title: Water uptake and ice nucleation by glassy organic aerosols

13 **Abstract**

14 Organic aerosol particles play a key role in climate by serving as nuclei for clouds and
15 precipitation. Their sources and composition are highly variable, and their phase state ranges
16 from liquid to solid under atmospheric conditions, affecting the pathway of activation to cloud
17 droplets and ice crystals. Due to slow diffusion of water in the particle phase, organic
18 particles may deviate in phase and morphology from their thermodynamic equilibrium state,
19 hampering the prediction of their influence on cloud formation. We overcome this problem by
20 combining a novel semi-empirical method for estimation of water diffusivity with a kinetic
21 flux model that explicitly treats water diffusion. We estimate timescales for particle
22 deliquescence as well as various ice nucleation pathways for a wide variety of organic
23 substances, including secondary organic aerosol (SOA) from the oxidation of isoprene, α -
24 pinene, naphthalene, and dodecane. The simulations show that in typical atmospheric
25 updrafts, glassy states and solid/liquid core-shell morphologies can persist for long enough
26 that heterogeneous ice nucleation in the deposition and immersion mode can dominate over
27 homogeneous ice nucleation. Such competition depends strongly on ambient temperature and
28 relative humidity as well as humidification rates and particle sizes. Reflecting difference in
29 glass transition temperature, hygroscopicity and atomic O/C ratio of SOA, naphthalene SOA
30 particles have the highest potential to act as heterogeneous ice nuclei. Our findings
31 demonstrate that kinetic limitations of water diffusion into organic aerosol particles are likely
32 to be encountered under atmospheric conditions and can strongly affect ice nucleation
33 pathways. For the incorporation of ice nucleation by organic aerosol particles into
34 atmospheric models, our results demonstrate a demand for model formalisms that account for
35 the effects of molecular diffusion and describe ice nucleation onsets not only as a function of
36 temperature and relative humidity, but also include updraft velocity, particle size and
37 composition.

38 1 Introduction

39 Atmospheric aerosol particles influence climate through affecting the earth's radiation budget
40 directly by scattering and absorbing light, and indirectly by acting as nuclei for cloud droplets
41 and ice crystals (Yu et al., 2006; Andreae and Rosenfeld, 2008; IPCC, 2013). Ice nucleation is
42 an important pathway for high-altitude cirrus cloud formation and it occurs either
43 homogeneously in liquid aerosol particles or heterogeneously in the presence of active ice
44 nuclei (IN), which are solid particles that facilitate nucleation. Homogeneous ice nucleation
45 generally requires high supersaturations in aqueous aerosol droplets, occurring at ice
46 saturation ratios of $S_{\text{ice}} \geq 1.4$ (Koop et al., 2000). Only a small fraction of atmospheric aerosol
47 particles act as IN below this homogeneous ice nucleation threshold (DeMott et al., 2003;
48 Cziczo et al., 2013). Heterogeneous ice nucleation can occur via several pathways such as
49 deposition nucleation, i.e. deposition of gaseous water molecules to form crystalline ice on a
50 solid IN, or immersion freezing, which describes nucleation induced by IN immersed in
51 supercooled aqueous droplets (Pruppacher and Klett, 1997; Hoose and Möhler, 2012).

52 Organic aerosol particles are ubiquitous and abundant in the atmosphere, but traditionally are
53 not referred to as effective IN when compared to dust or biological particles (see Hoose and
54 Möhler (2012) and references therein). More recently, however, several laboratory studies
55 have shown that glassy organic particles can act as IN at low-temperature cirrus conditions in
56 the deposition mode or at slightly elevated temperatures in the immersion mode (Murray et
57 al., 2010; Wagner et al., 2012; Wang et al., 2012; Wilson et al., 2012; Baustian et al., 2013;
58 Schill et al., 2014), in agreement with inferences from field data (Froyd et al., 2010; Knopf et
59 al., 2010; Knopf et al., 2014). This IN ability has been observed for a number of different
60 types of particles composed of pure organic substances such as simple sugars and acids
61 (Murray et al., 2010; Wagner et al., 2012; Wilson et al., 2012; Baustian et al., 2013) and
62 biomass burning marker compounds (Wagner et al., 2012; Wilson et al., 2012), for (phase-
63 separated) organic-inorganic mixtures (Wagner et al., 2012; Wilson et al., 2012; Baustian et
64 al., 2013; Schill and Tolbert, 2013), as well as for SOA particles derived from aromatic VOCs
65 (Wang et al., 2012) or emerging from aqueous phase reactions (Schill et al., 2014). It has also
66 been proposed recently that formation of highly porous structures upon atmospheric freeze-
67 drying could enhance the IN ability of organic aerosol particles (Adler et al., 2013).

68 These observations suggest a connection between particle phase state and the resulting
69 predominant ice nucleation pathway (Murray et al., 2010). Organic aerosol particles can adopt

70 liquid, semisolid or solid states, or may even exhibit mixed phases, depending on composition
71 and ambient conditions (Mikhailov et al., 2009; Koop et al., 2011; Vaden et al., 2011; Kuwata
72 and Martin, 2012; Perraud et al., 2012; Song et al., 2012; You et al., 2012; Renbaum-Wolff et
73 al., 2013; Kidd et al., 2014). SOA particles are expected to be liquid at high temperature and
74 high humidity, but are very likely to exhibit a highly viscous semisolid or even glassy state at
75 low temperature and low humidity (Virtanen et al., 2010; Saukko et al., 2012; Renbaum-
76 Wolff et al., 2013; Shiraiwa et al., 2013a). For example, typical α -pinene derived secondary
77 organic aerosol particles are expected to be in a glassy state below about 260 K at 30 %
78 relative humidity, whereas at a higher humidity of 80 %, such glass transition is expected at
79 approximately 215 K (Koop et al., 2011). Glassy states are characterized by viscosities greater
80 than 10^{12} Pa s, corresponding to diffusion time scales within these particles that can exceed
81 days or even years (Shiraiwa et al., 2011; Koop et al., 2011; Zhou et al., 2013). Water uptake
82 into glassy aerosols has been shown to occur slowly and to proceed gradually with increasing
83 relative humidity (Mikhailov et al., 2009; Tong et al., 2011; Zobrist et al., 2011; Bones et al.,
84 2012; Price et al., 2014).

85 Hence, several competing processes can occur in glassy organic aerosol particles during
86 updraft of an air parcel: Heterogeneous ice nucleation in the deposition mode onto the glassy
87 solid aerosol surface; diffusion of water into the particle, inducing a gradual phase transition
88 towards the liquid state; and immersion freezing during the transition between both states. In
89 order to determine those atmospheric conditions at which one of these processes dominates,
90 we employ a numerical aerosol diffusion model based on the kinetic multi-layer model for
91 gas-particle interactions in aerosols and clouds (KM-GAP), which explicitly treats mass
92 transport of water molecules in the gas and particle phases (Shiraiwa et al., 2012). Due to
93 experimental constraints associated with very long observation times, parameterizations for
94 water diffusivity in glassy organic material are sparse and hence are only known for a few
95 model compounds. Therefore, water diffusivity in SOA materials from various biogenic and
96 anthropogenic precursors are deduced from water diffusivity parameterizations of model
97 compounds using a semi-empirical physico-chemical model of water diffusion in glass-
98 forming aqueous organics.

99

100 **2 Modelling approach**

101 **2.1 Numerical diffusion model**

102 The numerical diffusion model employed in this study is based on the kinetic multi-layer
103 model for gas-particle interactions in aerosols and clouds, KM-GAP (Shiraiwa et al., 2012).
104 KM-GAP consists of multiple model compartments and layers, respectively: gas phase, near-
105 surface gas phase, sorption layer, surface layer, near-surface bulk, and a number of n bulk
106 layers (cf. Fig. S1 in the supplementary material). The following processes are considered in
107 KM-GAP: gas phase diffusion, gas-surface transport, surface-bulk transport, and bulk
108 diffusion. The bulk layers can either grow or shrink in response to mass transport. The initial
109 bulk layer sizes are chosen small enough to ensure numerical convergence (usually 100-750
110 layers), but are not allowed to fall below the molecular length scale (~ 0.3 nm).

111 The model was complemented by modules predicting homogeneous ice nucleation as a
112 function of water activity according to Koop et al. (2000), heterogeneous ice nucleation at a
113 pre-defined ice supersaturation level, and it considers Kelvin effects. Moreover, a few further
114 conceptual changes have been introduced to the original KM-GAP, including a more explicit
115 treatment of gas diffusion, composition-based bulk diffusion and a mechanism of surface-to-
116 bulk transport facilitated by surface-adsorbed water, as detailed in the following sections.
117 Parameterizations of composition-dependent density, water activity and bulk diffusivity for
118 the sucrose/water system have been adopted from Zobrist et al. (2011). A detailed description
119 of the gas diffusion scheme and a list of all employed parameterizations are provided as
120 supplementary material.

121 In this study, the model is used to simulate an atmospheric updraft situation by following a
122 preselected trajectory in temperature, relative humidity and pressure. It tracks the chemical
123 composition of an amorphous aerosol particle as a function of time and depth below the
124 particle surface in discretized layers, providing concentration profiles of water and organics at
125 any given time. The equilibrium composition is calculated through a water activity
126 parameterization that translates ambient relative humidity into equilibrium mass fractions of
127 the bulk constituents. Mass fluxes from the far-surface into the near-surface gas phase, onto
128 the particle surface, into as well as between bulk layers are coupled in flux-based differential
129 equations, which are solved with an ordinary differential equation solver using Matlab
130 software (ode23tb).

131 2.1.1 Ice nucleation modules

132 Besides water diffusion, the model is able to simulate ice nucleation and growth. However,
133 the initial numerical solution of the differential equations treats merely water uptake into the
134 particle. The model registers an ice nucleation event when all necessary conditions in ambient
135 relative humidity and water activity are satisfied. From this point onwards, the model
136 simulates ice crystal growth by deposition of water molecules from the gas phase.

137 For homogeneous ice nucleation, a stochastic approach based on classical nucleation theory
138 has been chosen. An ice nucleation event is triggered when the probability of the particle
139 being liquid (P_{liq}) falls below 50 %. P_{liq} is the product of the individual probabilities in all n
140 layers, using the homogeneous nucleation rate coefficient for each layer $J_{\text{hom},n}$ as
141 parameterized by Koop et al. (2000). The nucleation rate then translates into P_{liq} by
142 multiplication with layer volume V_n and (numerical) integration time step dt :

$$P_{\text{liq,tot}}(t) = \int_{t_0}^t \prod_{n=1}^L (1 - J_{\text{hom},n}(t) \cdot V_n(t)) dt \quad (1)$$

143 Heterogeneous nucleation is assumed to occur once a certain freezing threshold is exceeded.
144 In this work, we distinguish between heterogeneous ice nucleation thresholds for sucrose and
145 SOA, which have been shown to occur at different ice supersaturations, as summarized by
146 Schill et al. (2014). For sucrose, we apply a linear fit to nucleation data from Baustian et al.
147 (2013), whereas for SOA we fit the nucleation data of naphthalene SOA from Wang et al.
148 (2012) and those of aqSOA from Schill et al. (2014). The fit results are shown in Fig. A1 in
149 Appendix A.

150 To distinguish between deposition and immersion freezing, additional criteria are employed.
151 For deposition nucleation, the necessary condition is solidness of the outermost layer of the
152 particle, requiring the water activity to be below the quasi-equilibrium glass transition point.
153 In case of immersion mode nucleation, a 1 nm thick region in the near-surface bulk is
154 required to be entirely liquefied before nucleation can occur in the immersion mode. For this
155 purpose, a 2 nm thick region below the particle surface is finely resolved by multiple bulk
156 layers (cf. Fig. S1).

157 2.1.2 Bulk diffusion and bulk layer mixing

158 Bulk diffusion of water is treated as kinetic flux $J_{bk,bk\pm 1}$ from one bulk layer (bk) to the next
159 ($bk\pm 1$). Because layer thickness is not allowed to fall below molecular resolution,
160 concentrations in adjacent layers can differ significantly. As in Zobrist et al. (2011), this
161 heterogeneity is accounted for with a virtual mixing scheme for the determination of bulk
162 diffusivities between layers. In this scheme, the composition of a mixture of two subsequent
163 bulk layers is determined and the bulk diffusion coefficient calculated according to the
164 effective composition along the diffusion path. Scenarios with very low diffusivities and
165 hence steep concentration gradients thus lead to situations in which a liquefied layer (high
166 bulk diffusivity of water, D_{H_2O}) “softens” the subsequent glassy layer (low D_{H_2O}), facilitating
167 further diffusion. Such a process can be seen analogously to a dissolution process, in which
168 the glassy matrix dissolves into nearby water-rich regions.

169 Diffusion of the organic matrix has been neglected for this study, because the organic
170 molecules investigated here can be expected to diffuse much slower than water molecules.
171 Also, in the glassy state, the organic molecules diffuse on a much longer timescale compared
172 to the experimental time scale of minutes to hours [cf. Shiraiwa et al. (2011), Koop et al.
173 (2011)].

174 2.1.3 Surface monolayers and surface softening

175 The original KM-GAP uses a double monolayer approach to describe the particle surface,
176 comprising a sorption layer and a quasi-static surface layer. In this study the quasi-static
177 surface layer was replaced by a near-surface volume layer similar to that used in Shiraiwa et
178 al. (2013a), which is more suitable for systems with low diffusivity.

179 Surface-adsorbed water can lead to softening of the solid surface (Koop et al., 2011), thereby
180 facilitating exchange between surface and first near-surface bulk layer. In the model, this is
181 accounted for by introducing a surface softening scheme that estimates the surface-to-bulk
182 transport rate by mixing a hypothetical water monolayer with a hypothetical bulk monolayer
183 containing water and bulk material. Using the momentary molar fractions of water (x_{b1,H_2O})
184 and organics ($x_{b1,org}$) of the near-surface bulk layer, the effective surface coverages of water
185 (θ_{ss,H_2O}) and organics ($\theta_{ss,org}$) at the surface bulk layer can be described as:

$$\theta_{ss,i} = \frac{x_{b1,i} \cdot \sigma_i}{x_{b1,org} \cdot \sigma_{org} + x_{b1,H2O} \cdot \sigma_{H2O}} \quad (2)$$

186 where σ_i is the molecular cross section of species i [i.e. water (H₂O) or organics (org)],
 187 respectively. The weight fraction of organics in the “softened” surface is then given by:

$$w_{ss,org,mix} = \frac{\frac{\theta_{ss,org}}{\sigma_{org}} \cdot M_{org}}{\frac{\theta_{ss,org}}{\sigma_{org}} \cdot M_{org} + \left(\frac{\theta_{ss,H2O} + 1}{\sigma_{H2O}}\right) \cdot M_{H2O}} \quad (3)$$

188 where M_{org} and M_{H2O} are the molar mass of organics and water. This process facilitates the
 189 initial water uptake into a glassy particle and leads (in most cases) to a sub-surface layer that
 190 is in equilibrium with the surrounding gas phase. In the temperature range relevant for
 191 immersion freezing, liquefaction of the surface was always obtained at the quasi-equilibrium
 192 glass transition point due to the surface softening mechanism. At lower temperatures however
 193 (deposition regime), the particle surface was not always in quasi-equilibrium with ambient
 194 humidity.

195

196 **2.2 Estimation of water diffusivity in SOA**

197 For model systems other than sucrose/water, no direct parameterization of water diffusivity in
 198 the full atmospherically relevant temperature and composition range is available to date. For
 199 compounds chemically similar to sucrose (i.e. organic polyols and acids), we present a
 200 scheme that enables estimation of bulk diffusivity data from glass transition and
 201 hygroscopicity data. Bulk diffusivity of water is parameterized using a Vogel-Fulcher-
 202 Tamman (VFT) approach (Vogel, 1921; Fulcher, 1925; Tamman and Hesse, 1926). The
 203 estimation scheme utilizes the structure of the VFT equation, Eq. (S9), and the physical
 204 interpretation of its parameters. The method can be described by the following set of
 205 assumptions:

- 206 1. Two similar organic substances act similar in the way they approach the glass
 207 transition and thus have a similar fragility: $B_{org,1} \approx B_{org,2}$.
- 208 2. The same two substances have a similar diffusion coefficient in the high temperature
 209 limit: $A_{org,1} \approx A_{org,2}$.

210 3. A difference in glass transition temperatures between the two substances indicates a
211 difference in Vogel temperatures of same direction and (relative) magnitude

$$\frac{T_{0,\text{org},1}}{T_{0,\text{org},2}} \approx \frac{T_{g,\text{org},1}}{T_{g,\text{org},2}} \quad (4)$$

212 Thus, diffusivities within an organic substance can be estimated by knowledge of its glass
213 transition curve relative to a known standard with similar chemical functionality. This
214 approach requires knowledge of three parameters for inferring water diffusivity over the full
215 temperature and composition range: the hygroscopicity coefficient κ_{org} , the glass transition
216 temperature of the pure organic $T_{g,\text{org}}$ and the Gordon-Taylor coefficient k_{GT} of the aqueous
217 organic mixture. For justification, more information on this procedure and a description of
218 how the required input parameters are obtained, see Appendix A. For validation of the
219 estimation scheme, we provide applications to literature ice nucleation experiments in
220 Appendix B.

221 **3 Results and discussion**

222 **3.1 Particle Morphology**

223 We investigate ice nucleation in glassy organic aerosols induced by changing ambient
224 conditions during the updraft of an air parcel. In updraft events, adiabatic cooling leads to a
225 decrease in temperature and a corresponding increase of relative humidity (RH).
226 Humidification of air leads to water uptake into the particle phase, causing a humidity-
227 induced phase transition that for glassy aerosol particles has been termed *amorphous*
228 *deliquescence* (Mikhailov et al., 2009). This process is often kinetically limited by diffusion
229 of water in the particle phase (Zobrist et al., 2011), so that a particle can be out of equilibrium
230 when the time scale of humidification is shorter than that of diffusion.

231 Amorphous deliquescence is a self-accelerating process since water acts as a plasticizer in the
232 organic matrix (Mikhailov et al., 2009; Zobrist et al., 2011): Water molecules taken up by the
233 particle reduce the particle's viscosity and, hence, increase bulk diffusivity locally, thus
234 accelerating the uptake of further molecules. The microphysical consequences of this
235 mechanism are illustrated in Fig. 1, which shows the temporal evolution of particle
236 morphology of a glassy organic aerosol particle exposed to a gradual increase in relative
237 humidity (simulated atmospheric updraft, see also Movie S1). The quasi-equilibrium glass
238 transition of the aqueous organic, RH_g , is shown in grey. With “quasi-equilibrium glass
239 transition“, we denote the conditions under which a binary organic-water system would
240 undergo amorphous deliquescence when humidification occurs sufficiently slow so that
241 equilibrium between ambient RH and water activity is always maintained. Humidification
242 may be fast enough to cause a difference in phase state from equilibrium: Water activity,
243 colour-coded from dark blue (low water activity) to light blue (high water activity), trails
244 behind ambient RH due to kinetic limitations in water diffusivity (Koop et al., 2011). Note
245 that when using a constant D_{H_2O} , diffusion gradients appear less pronounced (cf. Fig. S2 and
246 Movie S2). Hence, self-accelerating water diffusion leads to a sharpening of the diffusion
247 gradient that can be close to the molecular length scale (Zobrist et al., 2011).

248 Several morphological stages can be distinguished during the humidification process in Fig. 1.
249 Starting from a homogeneous, glassy particle (1), an increase in RH first leads to liquefaction
250 of a thin outer layer and emergence of a core-shell morphology (2). This liquid outer layer
251 grows in equilibrium with ambient relative humidity and also extends towards the particle

252 centre by diffusion of water into the glassy organic matrix (3), leading to shrinkage of the
253 residual glassy core until the particle is fully deliquesced (4). Thus, during the continuous
254 amorphous deliquescence process two characteristic instants can be distinguished, each
255 occurring at a different humidity: We define the *Partial Deliquescence Relative Humidity*
256 (PDRH) as the point where a thin aqueous outer shell of the particle is homogeneously mixed
257 and the shell's water activity is larger than that of the quasi-equilibrium glass transition. In
258 this study we set the thickness of this surface shell to 1 nm, corresponding to about 5
259 monolayers of water. We define the *Full Deliquescence Relative Humidity* (FDRH) as the
260 point where its water activity corresponds to that of a liquid (i.e. it is larger than that of the
261 quasi-equilibrium glass transition) and the water activity gradient from the surface to the
262 particle core is less than 5 %. Note that in the case of a sufficiently slow updraft, both PDRH
263 and FDRH would occur at RH_g . In fact, the KM-GAP simulations suggest that, with updraft
264 velocities typical for atmospheric conditions (e.g. $0.01 - 10 \text{ m s}^{-1}$), PDRH often coincides
265 with RH_g . In contrast, FDRH often extends far into the liquid region of the phase diagram,
266 indicating the importance of kinetic limitations and implying that particles can contain glassy
267 cores even at relative humidities above RH_g due to slow water diffusion.

268 **3.2 Ice nucleation regimes**

269 Next, we investigate by kinetic model simulations the competition between amorphous
270 deliquescence and ice nucleation during an atmospheric updraft. For our initial calculations
271 we use sucrose as a proxy for organic aerosols since detailed physico-chemical
272 parameterizations for water diffusivity, the RH-dependent equilibrium composition as well as
273 glass transition data are available (Zobrist et al., 2011). The heterogeneous ice nucleation
274 onset (RH_{het}) for sucrose was obtained from ice nucleation experiments by Baustian et al.
275 (2013) and is shown as brown dashed lines in Fig. 2. Here we use the ice saturation ratio S_{ice}
276 as an indicator of humidity because it scales with RH according to $S_{\text{ice}} = p_{\text{liq},0}(T) / p_{\text{ice}}(T) \cdot \text{RH}$,
277 but is also a more direct indicator of the supersaturation of ice.

278 Figure 2A shows results obtained with KM-GAP simulating the updraft of 100 nm sucrose
279 particles for a wide range of temperatures. Each simulated trajectory started at ice saturation
280 ($S_{\text{ice}} = 1$), as is often the case for cloud chamber or environmental cell experiments (Murray et
281 al., 2010; Wang et al., 2012). Temperature was decreased so that the resulting humidification

282 rate was constant at 1 \% RH min^{-1} , corresponding to an atmospheric updraft of about 0.2 m s^{-1} ,
283 1 , typical of atmospheric gravity waves (Jensen et al., 2005).

284 As expected FDRH of sucrose particles, indicated by the red solid line, occurs significantly
285 above RH_g at all temperatures. The intersection of RH_{het} with RH_g defines the upper
286 temperature limit for deposition nucleation. Below this temperature, a sucrose particle is a
287 glassy solid when RH_{het} is reached, and hence deposition ice nucleation may occur. Above
288 this temperature, the particle is partially deliquesced when approaching RH_{het} and the glassy
289 core of the particle may act as an IN for immersion freezing. The upper limit of the immersion
290 freezing regime is given by the intersection of RH_{het} with the FDRH line. Above this
291 temperature, particles are already fully deliquesced once RH_{het} is reached. Hence, these
292 particles do not nucleate ice heterogeneously and freeze only at the homogeneous ice
293 nucleation limit (green dashed line; Koop et al., 2000). Finally at $\sim 232 \text{ K}$, the homogeneous
294 ice nucleation limit coincides with water saturation (solid black line) and above this
295 temperature the aerosol particles activate into cloud droplets consisting of supercooled water,
296 thus representing the upper limit of the homogeneous ice nucleation regime.

297 The delay between the nominal quasi-equilibrium glass transition RH_g and the actual full
298 deliquescence at FDRH is governed by the competition between humidification rate
299 (synonymous to updraft velocity) and timescale for water diffusion within the particle bulk.
300 FDRH will shift towards higher relative humidities when higher humidification rates are
301 employed, as shown in Fig. 2B. For example, increasing the rate of humidification to 10 \%
302 RH min^{-1} , a value corresponding to an updraft velocity of about 2 m s^{-1} and commonly
303 reached in convective updrafts (Jensen et al., 2005), shifts the FDRH line upwards (solid dark
304 blue line) and thus its intersection with the RH_{het} line towards higher temperatures.
305 Accordingly, decreasing the updraft velocity to 0.02 m s^{-1} , a value found in large-scale,
306 synoptic updrafts (Jensen et al., 2005), leads to FDRH (solid light blue line) much closer to
307 the quasi-equilibrium glass transition RH_g . Moreover, an increase in particle size delays the
308 deliquescence process (indicated by the solid purple line), since it increases the timescale of
309 diffusion. The range of the immersion freezing regime thus strongly depends on ambient
310 conditions and is extended towards higher temperatures in fast updrafts and for large particles.

311 Laboratory ice nucleation measurements with sucrose particles (Baustian et al., 2013) are
312 used to validate our model calculations of ice nucleation regimes in Fig. 2C. Baustian et al.
313 used optical microscopy in conjunction with a cold stage to detect ice nucleation on glassy

314 sucrose particles (4 μm diameter) during humidification (1 % RH min^{-1}), leading to the
315 nucleation onsets shown in Fig. 2C (brown markers). A range of simulations mimicking the
316 experimental conditions at different starting temperatures leads to a continuous FDRH curve
317 (solid blue line) over the entire temperature range. For details on the calculations see
318 Appendix B. The modelled FDRH curve correctly confines the region below which
319 heterogeneous ice nucleation is observed in the experiments. Based on our calculations, the
320 experimental data points below RH_g (full brown circles) can be assigned to the deposition
321 nucleation regime, whereas points between RH_g and FDRH (open brown circles) can be
322 assigned to immersion freezing. Additional analyses for validation have been performed for
323 other types of organic particles (Figs. B1 and B2).

324 **3.3 Biogenic and anthropogenic SOA**

325 In order to apply our kinetic model to ice nucleation in secondary organic aerosol (SOA),
326 estimates of $D_{\text{H}_2\text{O}}$ in SOA material have been inferred. Four major SOA precursors were
327 chosen to represent biogenic and anthropogenic origin, respectively: α -pinene and isoprene,
328 as well as naphthalene and dodecane. Each of these SOA is represented by a choice of marker
329 compounds taken from the literature (cf. Table S1). Water diffusivities are estimated utilizing
330 the scheme described in Sect. 2.2. The heterogeneous ice nucleation onset (RH_{het} , brown
331 dashed line) for SOA was obtained from laboratory measurements by Wang et al. (2012) and
332 Schill et al. (2014) as derived in Fig. A1. Hygroscopicities of the various SOA were taken
333 from Lambe et al. (2011), who suggested that κ_{org} can be parameterized independently of SOA
334 type as function of O/C ratio. In all simulations, particles of 100 nm diameter were humidified
335 at a rate of 1 % RH min^{-1} .

336 Figure 3A shows the simulation results of FDRH for all four precursor types. Naphthalene
337 SOA is observed to be fully deliquesced latest due to the high estimated glass transition
338 temperature and low hygroscopicity (cf. Table A1), followed by α -pinene and isoprene.
339 Dodecane SOA showed the earliest deliquescence, reflecting the low glass transition
340 temperature of pure dodecane SOA of ~ 210 K. By comparison of FDRH with measured RH_{het}
341 on SOA, compound-specific upper temperature limits for heterogeneous ice nucleation on
342 SOA particles can be determined (arrows on x-axis, values are given in Table S2).
343 Uncertainty estimates for FDRH and RH_g of all four precursors classes are given in Fig. S4.

344 For the calculations in Fig. 3A, we chose an average oxidation state typically observed for
345 SOA from the respective precursor. The atomic oxygen to carbon ratio (O/C) increases upon
346 chemical ageing, thereby affecting hygroscopicity (Lambe et al., 2011) and glass transition
347 temperature (Fig. A2). The resulting effects of chemical ageing on modelled FDRH are
348 shown exemplarily for α -pinene and dodecane SOA in Fig. 3B and C, respectively. For α -
349 pinene SOA (B), a higher O/C results in hardening of the organic material with ageing,
350 leading to a FDRH increase, whereas for dodecane SOA (C) a higher O/C results in softening,
351 thus leading to earlier deliquescence and a FDRH decrease.

352 The observed effects can be explained by the competition between a simultaneous increase of
353 hygroscopicity with O/C and an increasing glass transition temperature of the pure organic
354 matrix due to stronger molecular interactions in the highly oxidized organic material. A
355 higher glass transition value enhances the rigidity of the pure organic matrix, whereas a
356 higher hygroscopicity enhances the amount of water taken up by the aqueous organic mixture
357 at a given humidity and thus its plasticizing effect.

358 Figure 4 illustrates this competition by displaying estimated characteristic timescales of water
359 diffusion in 100 nm diameter SOA particles at 220 K as a function of hygroscopicity (κ_{org})
360 and glass transition temperature of the pure organic matrix ($T_{\text{g,org}}$). Dotted contour lines show
361 characteristic mass transport times associated with the diffusion coefficient $D_{\text{H}_2\text{O}}$ (Shiraiwa et
362 al., 2011). Coloured oval shapes indicate estimated ranges of κ_{org} and $T_{\text{g,org}}$ for the four SOA
363 precursor classes, for three different oxidation states each (cf. Table A1). The arrows pointing
364 from the lowest to the highest oxidation state reveal that both κ_{org} and $T_{\text{g,org}}$ increase with O/C.
365 The slope of these arrows when compared to the slope of the contour lines indicates whether a
366 compound undergoes hardening (steeper slope) or softening (shallower slope) during the
367 ageing process. Apparently, both biogenic SOA types undergo hardening upon ageing,
368 whereas the two anthropogenic SOA types undergo softening, with the strongest effects for
369 pinene and dodecane SOA.

370 The area between 1 s and 1 h represents the time scale of atmospheric updraft processes. For
371 SOA in this range, diffusion processes occur on the same time scales as typical air parcel
372 updrafts and the predominant cloud formation process depends strongly on atmospheric
373 conditions. All four SOA types fall within or beneath this range, indicating the importance of
374 the actual updraft velocity for ice nucleation on glassy aerosols. But it is also obvious that

375 SOA particles from naphthalene are most likely to be subject to kinetic effects and may thus
376 act as IN.

377 **3.4 Model uncertainties**

378 The model results presented in this study are subject to various types of uncertainty. Among
379 these are uncertainties arising from model assumptions such as the validity of first-order
380 Fickian diffusion and the applied schemes for bulk mixing and surface softening (Sects. 2.1.2
381 and 2.1.3). At present there is a lack of fundamental chemical and physical knowledge for
382 describing these processes in aqueous binary or multicomponent systems. We note, however,
383 that the approach taken here is in agreement with the sparse data on water diffusivities in
384 aqueous organic systems (Zobrist et al., 2011; Shiraiwa et al., 2013b; Lienhard et al., 2014;
385 Price et al., 2014). Model results obtained for aqueous sucrose (Fig. 2) are expected to be
386 reliable because the thermodynamic and kinetic parameters of this benchmark system are well
387 studied and agree within the literature (e.g. Zobrist et al., 2011; Price et al., 2014); on the
388 other hand, model results obtained for SOA (Fig. 3) are subject to larger uncertainties as
389 detailed in the following.

390 The model neglects liquid-liquid phase separation in the aqueous organic phase (You et al.,
391 2014) by assuming that all SOA components are miscible with water over the entire
392 concentration and temperature range. We note that for SOA types that typically show only
393 low O/C ratios (e.g. SOA from long chain aliphatic precursors such as dodecane), insoluble
394 fractions may become important for ice nucleation (see discussion in Sect. B2).

395 Volatilization of organic material has not been included in the calculations presented above
396 since vapour pressures of typical SOA marker compounds are low under the low temperature
397 conditions employed in this study (Huisman et al., 2013; O'Meara et al., 2014).

398 Self-diffusion of SOA material has been neglected as diffusion time scales of large organic
399 molecules exceed those of small guest molecules in the SOA matrix by orders of magnitudes
400 (Koop et al., 2011; Shiraiwa et al., 2011).

401 Minor model uncertainty comes from parameters determining the volume concentration of
402 organic molecules at a given organic mass fraction, i.e. average molar mass M_{org} of the
403 organics and density of the aqueous organic mixture (cf. Table S3). Variation by 100 g mol^{-1}
404 in M_{org} showed no effect on model results, varying ρ_{org} by 0.1 g cm^{-3} showed only a slight
405 influence on aerosol deliquescence humidity on the order of 1 % RH.

406 The arguably largest source of uncertainty is insufficient knowledge of the thermodynamic
407 input parameters required for the diffusivity estimation scheme (κ_{org} , $T_{\text{g,org}}$, k_{GT} , cf. Appendix
408 A). In addition to the general assumptions made in that scheme and the uncertainties in the
409 sucrose parameterization used within the diffusivity estimation scheme, uncertainties in input
410 parameters propagate into an uncertainty in $D_{\text{H}_2\text{O}}$, which we assess in Figs. S4 and S6. Figure
411 S4 shows the uncertainty for each specific SOA precursor and a particular O/C ratio by
412 propagating the maximum deviation estimates in κ_{org} and $T_{\text{g,org}}$ given in Table A1. Figure S6
413 shows the full uncertainty towards single model input parameters irrespective of precursor or
414 oxidation state. Among these, κ_{org} seems to be the largest source of uncertainty as the model
415 results are sensitive towards κ_{org} and its numerical value subject to a rather large variability
416 for atmospherically relevant organic substances (Koop et al., 2011; Lambe et al., 2011;
417 Rickards et al., 2013). Due to lack of consistent experimental data, a constant κ_{org} is used in
418 this study to parameterize hygroscopicity over the entire concentration and temperature range.

419 Thus, laboratory experiments that directly probe diffusivity within SOA at room temperature
420 and also at low temperature are highly desirable, as it has been done for sucrose and few other
421 single-compound proxies (Tong et al., 2011; Zobrist et al., 2011; Bones et al., 2012; Lienhard
422 et al., 2014; Price et al., 2014). Moreover, experiment-based water activity parameterizations
423 over a large temperature range are needed, because at least some water-soluble organic
424 oligomers/polymers show a strong temperature dependence of water activity for aqueous
425 mixtures of constant composition (Zobrist et al., 2003). Both such improvements would
426 reduce the model uncertainty in future modelling studies substantially.

427 Another type of uncertainty arises from uncertainty in heterogeneous ice nucleation onsets.
428 To date, little is known about the exact microphysical mechanism by which amorphous
429 organics nucleate ice heterogeneously (Wagner et al., 2012; Marcolli, 2014; Schill et al.,
430 2014). Reported ice nucleation onsets of glassy particles span wide ranges and are most likely
431 substance or substance class-specific (Wilson et al., 2012; Schill et al., 2014). Thus, further
432 laboratory experiments are needed that reveal details on the ice nucleation mechanism and
433 that allow predictions of ice nucleation ability for a wide variety of substances.

434

435 **4 Atmospheric implications of glassy organic IN**

436 Organic aerosols can induce cloud formation via many different pathways depending on
437 ambient conditions and composition. At high temperature and high humidity, liquid organic
438 particles can act as cloud condensation nuclei (CCN). At lower temperatures, they facilitate
439 formation of ice crystals. Figure 5 summarizes how the phase state and morphology of
440 atmospheric organic aerosol particles may vary upon changes in ambient relative humidity
441 (humidity-induced phase transitions). Upon humidifying, the phase state changes from
442 amorphous solid (glassy) over a partially-deliquesced state with a solid core residual coated
443 by a liquid shell to a fully-deliquesced liquid. Upon drying the transition may occur via an
444 inverse core-shell morphology, i.e. a liquid coated by a solid shell. Consequently, the particle
445 phase state determines the active ice nucleation pathway: Glassy solids can nucleate ice in the
446 deposition mode, partially deliquesced particles with core-shell morphologies may act as IN
447 in the immersion mode and liquid particles nucleate ice homogeneously, at significantly
448 higher ice supersaturation.

449 From the SOA types investigated in this study, aromatic SOA or highly aged α -pinene SOA
450 may persist in a glassy state to the highest temperatures and humidities and may thus facilitate
451 heterogeneous ice nucleation at temperatures of up to 225 K. Below 210 K, SOA from all
452 precursors are expected to be in the glassy state required for heterogeneous ice nucleation.
453 Our microphysical simulations suggest a potential anthropogenic influence of IN from
454 emission of aromatic VOCs and by providing high oxidative capacities in urban areas leading
455 to an increase of ice nucleation in and on glassy organic particles.

456 Compared to typical atmospheric IN such as dust, soot and biological particles, glassy organic
457 particles require temperatures below ~ 230 K to nucleate ice heterogeneously (Hoose and
458 Möhler, 2012). This restriction confines their atmospheric activity range to the upper
459 troposphere – lower stratosphere region since the glassy state is prevalent only up to
460 temperatures of about 200 – 240 K under typical atmospheric humidities ($S_{ice} \approx 1$), depending
461 on composition.

462 In this study we show a strong interplay between diffusion time scales in the atmosphere and
463 atmospheric updraft speeds: the stronger the updraft and the larger the particle size, the more
464 kinetic limitations delay the liquefaction of glassy particles. These findings also imply that an
465 ice nucleation onset determined in laboratory studies needs to be interpreted carefully in order
466 to apply it to realistic atmospheric parameters, i.e. humidification rate, particle size and

467 starting humidity. Kinetic limitations are already pronounced at the smallest atmospherically
468 relevant updraft velocities of 0.02 m s^{-1} . When humidification is fast (e.g. in convective
469 updrafts), the glassy state may persist well above its quasi-equilibrium boundaries. Our
470 simulations on sucrose and SOA particles suggest a shift of humidity-induced glass transition
471 to higher temperatures by about 5 K when updraft velocities are increased by a factor of 10.
472 Also, the history of an organic particle has effects on its water uptake properties: Particles that
473 were equilibrated at lower humidity are expected to deliquesce at higher ice supersaturation.
474 In situations where particles are both, equilibrated in dry air ($S_{\text{ice}} < 0.9$) and elevated quickly,
475 upper temperature limits for immersion freezing on glassy organics might reach much higher
476 values than the conservative estimates given in this study. Thus, also ice nucleation in mid-
477 altitude clouds may be affected by this heterogeneous ice nucleation pathway.

478 This study outlines the basic physico-chemical relations and makes a first attempt in
479 quantifying temperature limits for heterogeneous ice nucleation by four generic types of SOA,
480 but further laboratory and modelling studies are needed to provide a comprehensive set of
481 parameterizations to be used in atmospheric models. To assess the global importance of ice
482 nucleation by SOA particles and to quantify the associated aerosol effects on climate, studies
483 with large scale computational models are needed. As small scale kinetic processes cannot be
484 treated explicitly in these kinds of models, parameterizations are required that include
485 dependencies upon temperature, relative humidity, updraft velocity, particle size and
486 composition.

487 **Appendix A: Details on the estimation of bulk diffusivities from glass transition** 488 **and hygroscopicity data**

489 **A.1. Justification of the method**

490 Even though the estimation scheme described in Sect. 2.2 represents a rather crude estimation
491 of water diffusivities, it builds on basic physical principals: In solutions of chemically similar
492 organic substances (like the mixture of highly functionalized organic species in SOA), the
493 types of molecular interactions are mostly hydrogen bonds and dispersion interactions,
494 irrespective of the actual composition. Differences in diffusive properties are to a substantial
495 degree due to factors such as molar mass and shape, both of which directly affect the glass
496 transition temperature (Koop et al., 2011). The way by which the glass transition is
497 approached is not affected strongly by the substance type, as all organic compounds relevant
498 for SOA are *fragile* glass-formers (Angell, 1985). The proposed method is consistent with the
499 following previous studies:

500 Rampp et al. (2000) used NMR spectroscopy to determine water diffusion coefficients in
501 different carbohydrate matrices (sucrose, allosucrose, leucrose, trehalose) and fitted VFT
502 parameters to the temperature and concentration-dependent data sets. Overall, similar VFT
503 parameters A and B were found for these chemically similar substances, even though $D_{\text{H}_2\text{O}}$
504 seemed to depend strongly on organic mass fraction, thus supporting assumptions 1 and 2
505 above. The observed concentration dependence was described almost exclusively by a change
506 in T_0 , with only small trends in A and minor variation in B , possibly due to experimental error,
507 thus supporting assumption 3.

508 Angell (1997) investigated the correlation of Kauzmann temperatures T_k with Vogel
509 temperatures T_0 and found their ratio to be close to unity. The ratio of T_g to T_0 has been shown
510 to be confined to a narrow range between $1.07 < T_g/T_0 < 1.82$ for a wide variety of strongly
511 different substances. This ratio seems to be correlated in magnitude to the substances fragility
512 (i.e. VFT parameter B), with high fragilities implying high T_g/T_0 ratios. Reversely the
513 assumption of similar fragilities (assumption 2) directly points towards similar T_g/T_0 ratios
514 (assumption 3). Accordingly, deducing Vogel temperatures T_0 from glass transition properties
515 seems reasonable.

516 **A.2. Estimation of glass transition temperatures $T_{g,org}$**

517 The proposed estimation scheme enables the prediction of bulk diffusion coefficients only
518 from knowledge of glass transition values for the desired RH range. The glass transition curve
519 can be described by three parameters: the glass transition temperature of the pure molecular
520 compound $T_{g,org}$; the Gordon-Taylor constant k_{GT} of the aqueous organic mixture; and the
521 hygroscopicity κ_{org} for translating composition into water activity. $T_{g,org}$ exhibits a linear
522 correlation with melting point T_m , also known as the Boyer-Beaman rule (Koop et al., 2011).
523 T_m can be estimated by group contribution models with knowledge of its chemical structure.
524 We use the melting point prediction model of UPPER (Unified Physical Property Estimating
525 Relationships) as presented by Jain et al. (Jain and Yalkowsky, 2006; Jain et al., 2004).

526 Table S1 shows our choice of marker substances for four different types of SOA along with
527 molar mass, melting points predicted with UPPER and predicted glass transition values based
528 on the Boyer-Beaman rule. The SOA groups were chosen to include SOA from the most
529 commonly studied precursors and are derived from one specified precursor substance each.
530 The groups “ α -Pinene” and “Isoprene” represent SOA from biogenic origin, whereas
531 “Naphthalene” and “Dodecane” are our choice for precursors of anthropogenic origin.

532 The group “ α -Pinene” contains compounds characteristic for photooxidation and ozonolysis
533 of the biogenic SOA precursor α -pinene, which has been chosen as proxy for the different
534 monoterpene VOCs responsible for biogenic SOA formation. The list contains compounds
535 with the highest yields according to MCM-based simulations of Shilling et al. (2009) as well
536 as of Zuend and Seinfeld (2012), who also included two dimer substances. Furthermore, we
537 included 3-MBTCA, a highly oxidized pinene derivative found in ambient samples
538 (Szmigielski et al., 2007) as well as terpenylic acid, a tracer for rather fresh SOA, along with
539 two of its derivatives (Claeys et al., 2009).

540 The group “Isoprene” contains isoprene-derived compounds found in ambient and laboratory
541 aerosol as suggested by Surratt et al. (2006) and references therein. These authors also
542 proposed a high contribution of esterification products with 2-methylglyceric acid as
543 monomeric unit to SOA mass. Table S1 lists these oligomers up to the tetramer level, where
544 predicted glass transition values start to level off.

545 The group “Naphthalene” represents typical products originating from the oxidation of
546 anthropogenic aromatic precursors. Note that for highly functionalized aromatic compounds,

547 UPPER predicts unusually high values for T_m , which are inconsistent with observations. For
548 example, phthalic acid melts under decomposition (presumably anhydrate formation) at 403 K
549 (Lide, 2005), whereas UPPER suggests a melting point of about 539 K. For this reason, we
550 used only those naphthalene oxidation products for which literature melting points are known,
551 such as the substances given in Saukko et al. (2012) and a number of compounds listed in
552 Kautzman et al. (2010). Note that for the same reason we did not include oligomerization
553 products to the “Naphthalene” group. Oligomerization is however also expected for aromatic
554 SOA, shown e.g. by Kalberer et al. (2004), which would lead to higher $T_{g,org}$ (Koop et al.,
555 2011). For these reasons, our estimates for aromatic SOA materials may be regarded as a
556 conservative estimate.

557 The group “Dodecane” in Table S1 lists oxidized organics derived from the C12 straight
558 chain alkane to represent the family of similar compounds originating from aliphatic VOCs of
559 anthropogenic origin. The list is a selection from the comprehensive chemical mechanism in
560 Yee et al. (2012) and three compounds from those suggested by Zhang et al. (2014).

561 The resulting glass transition values are presented in Fig. A2 as a function of atomic O/C ratio
562 and a clear positive correlation is observed within each group of compounds. Such a
563 correlation between $T_{g,org}$ and O/C has been supported by recent T_g measurements of mixtures
564 of α -pinene derived oxidation compounds (Dette et al., 2014). In Fig. A2, the solid lines are
565 obtained by linear regressions of the glass transition values using a bisquare weighting
566 function and shaded areas are confidence intervals at the 1σ level. The chosen marker
567 compounds occupy compound-specific ranges of O/C values, which is in part due to a
568 different carbon number in the precursor molecule. To estimate a value characteristic for a
569 mixture of the single compounds, we choose three values of O/C ratios that are typical for the
570 respective group and take at each of those values the corresponding $T_{g,org}$ that arises from the
571 linear fit. The errors are then given by the extension of confidence bands at each point. The
572 results are shown in Table A1.

573

574 **A.3. Estimation of Gordon-Taylor constants k_{GT}**

575 Gordon-Taylor constants are necessary to estimate the glass transition temperatures of
576 compound mixtures. Zobrist et al. (2008) determined Gordon-Taylor constants for a variety of
577 atmospherically relevant substances and SOA proxies. However, data are sparse when
578 compared to the wide structural variety of compounds in SOA and no clear correlation can be

579 drawn from the molecular structure. For this reason, Koop et al. (2011) recommended the
580 usage of a mean Gordon-Taylor constant of $k_{GT} = 2.5 \pm 1$ (cf. Table A1). Figure S6 shows the
581 temperature dependence of FDRH in calculations similar to Figs. 2 and 3, this time using the
582 best guess parameters recommended in Koop et al. (2011). The uncertainty in FDRH that
583 arises from the given input parameter ranges is shown (grey shaded), but also the specific
584 uncertainty from varying k_{GT} between 1.5 and 3.5 is highlighted (orange shaded).

585

586 **A.4. Estimation of hygroscopicities κ_{org}**

587 The hygroscopicity of a compound can be expressed by a single parameter κ_{org} , which is
588 strongly correlated to its degree of oxidation (Petters and Kreidenweis, 2007; Lambe et al.,
589 2011). A typical value for κ_{org} in biogenic SOA particles collected in pristine rainforest
590 environments is 0.1 (Gunthe et al., 2009), which was also used by Koop et al. (2011) for their
591 estimation of glass transition values in biogenic SOA.

592 For estimation of κ_{org} , we use the parameterization of Lambe et al. (2011) that correlates the
593 O/C ratio of secondary organic material to its hygroscopicity, Eq. (A1).

$$\kappa_{org} = (0.18 \pm 0.04) * O/C + 0.03 \quad (A1)$$

594 Each SOA precursor class is assigned a typical O/C value from previous investigations of
595 marker compounds (cf. Fig A2) and results are shown in Table A1. With the knowledge of
596 $T_{g,org}$, k_{GT} and κ_{org} , the entire glass transition curves for the four SOA types can be calculated,
597 as visualized in Fig. S4. Dashed lines and grey shaded areas indicate ranges of uncertainty.

598

599 **A.5. Evaluation of the method**

600 For evaluation of the performance of the diffusivity estimation scheme, we compare estimated
601 diffusivity values with values obtained in experiments by Price et al. (2014). In these
602 experiments, D₂O-H₂O exchange in an organic matrix at constant temperature and humidity is
603 investigated by Raman spectroscopy. Figure S3 shows the experimentally determined D_{H_2O}
604 values for sucrose and levoglucosan in Price et al. (blue and purple markers) as well as the
605 D_{H_2O} parameterization from Zobrist et al. (2011) (blue solid line). D_{H_2O} in levoglucosan has
606 also been estimated with the diffusivity estimation scheme (purple solid line), utilizing input

607 parameters from Zobrist et al. (2008) ($T_{g,org} = 283.6$ K, $k_{GT} = 5.2$). Water activity has been
608 parameterized using the parameters in Table S4.

609 Experimental and estimated values coincide for the highest and lowest water activities but
610 differ under medium conditions due to the different curvature of the base parameterization
611 from Zobrist et al. that underlies all calculations. However, diffusivities differ only within at
612 most two orders of magnitude, which is a considerably small deviation compared to the large
613 set of approximations made here and the difference between experimental techniques.

614 **Appendix B: Application of the model to ice nucleation experiments in the** 615 **literature**

616

617 **B.1. Sucrose experiments**

618 Baustian et al. (2013) investigated sucrose particles deposited on a quartz substrate and
619 humidified inside an experimental flow cell. After cooling and drying below the glass
620 transition, particles with an average diameter of 4 μm were humidified by cooling at a rate of
621 0.1 K min^{-1} . Humidification was initialized below ice saturation ($S_{\text{ice}} < 0.9$). The resulting
622 heterogeneous ice nucleation onsets (brown circles) are shown in Fig. 2C along with the full
623 deliquescence relative humidity (FDRH, blue solid line) from multiple model runs (spacing: 2
624 K) mimicking the experimental conditions. Simulations below 215 K (left black square
625 marker) are found to nucleate in the deposition mode, whereas particles in runs between about
626 215 K and 238 K (right black square marker) are assumed to undergo immersion freezing.
627 This result is compliant with the experimental values, none of which exceeds a nucleation
628 temperature of 235 K. Above 238 K full deliquescence occurs before the ice supersaturation
629 required for heterogeneous ice nucleation (brown dashed line) is reached. Also, homogeneous
630 ice nucleation is not possible anymore below the water saturation limit according to Koop et
631 al. (2000; green dashed line), leaving no remaining ice nucleation pathway.

632

633 **B.2. Naphthalene SOA experiments**

634 Wang et al. (2012) generated SOA by oxidation of naphthalene by OH in a potential aerosol
635 mass (PAM) reactor, deposited the particles on glass slides and investigated the onsets of
636 water uptake and ice nucleation inside an ice nucleation cell that was mounted on a
637 microscope. Experimental results are shown in Fig. B1 for three different SOA oxidation
638 states: Low O/C (0.27) given in red, medium O/C (0.54) in green and high O/C (1.0) in blue.
639 For the comparing model simulations, we employ our diffusivity estimation scheme with the
640 glass transition parameterization for naphthalene given above. A humidification rate of 1 %
641 RH min^{-1} was employed and temperature varied accordingly to maintain a constant dew point.
642 In Fig. B1, the lines of full deliquescence relative humidity (FDRH) divide the measured
643 heterogeneous ice nucleation onsets into two groups, irrespective of the degree of oxidation
644 used in the simulation. Heterogeneous nucleation at or below 225 K is consistent with

645 simulation results (closed diamonds), whereas ice nucleation at or above 230 K cannot be
646 explained with the estimated water diffusion properties (open diamonds). According to the
647 model simulation, naphthalene SOA should be already deliquesced at temperatures and RH
648 where ice nucleation is still experimentally observed. The model simulations thus suggest that
649 a different ice nucleation mechanism that does not require organic material in a glassy state
650 was active in these experiments. Possibly, insoluble products from Naphthalene OH oxidation
651 remained solid in the otherwise fully deliquesced particle and nucleated ice heterogeneously
652 with lower efficiency. Such a process is not considered in the model, which does not resolve
653 single compounds and treats Naphthalene SOA as homogeneous mixture at all times.

654 The reliability of the method is confirmed by comparing experimental and modelled water
655 uptake onsets that show very good correlation. The modelled water uptake onset was defined
656 as the point where the particle diameter had increased by 100 nm to take into account the fact
657 that experimental onsets were determined by visible inspection under a light microscope.

658

659 **B.3. Citric acid experiments**

660 Murray et al. (2010) observed the process of heterogeneous ice nucleation on glassy aerosols
661 by investigating citric acid particles in the AIDA cloud chamber. The experimentally
662 determined onsets of heterogeneous (orange diamonds) and homogeneous ice nucleation
663 (green circles) are shown in Fig. B2 along with results of simulations mimicking the
664 experimental conditions. In the calculations, we assumed a particle diameter of 150 nm and a
665 humidification rate of 12 % RH min⁻¹, corresponding to a cooling rate of 1-2 K min⁻¹.
666 Humidification was initiated at $S_{ice} = 1$ since the cloud chamber walls were covered with ice
667 during the initial cooling process. We performed two series of simulations for two different
668 water activity parameterizations available in the literature. According to the parameterization
669 in Lienhard et al. (2012) (dashed lines), heterogeneous nucleation occurs exclusively above
670 the (equilibrium) glass transition relative humidity RH_g and thus in the immersion freezing
671 regime. With the parameterization from Koop et al. (2011) (solid lines), equilibrium glass
672 transition and full deliquescence occur at later stages in the humidification process. According
673 to this data, only the experimental data point at about 206 K would have occurred in the
674 immersion mode.

675 At 212 K, ice nucleation occurs only homogeneously in Murray's experiments, indicated by
676 the much later ice nucleation onset. The humidification run started with liquid aerosol

677 particles that showed retarded deliquescence, but were not able to nucleate ice
678 heterogeneously.

679 **Author contributions**

680 T. B., M. S., U. P. and T. K. designed research; T. B., M. S. and T. K. developed the model;
681 T. B. performed research; T. B. and T. K. analysed simulation data; T. B., M. S., U. P. and T.
682 K. wrote the paper.

683

684 **Acknowledgements**

685 This work was funded by the Max Planck Society (MPG), the Deutsche
686 Forschungsgemeinschaft through the Ice Nuclei Research Unit INUIT (FOR1525, Grant KO
687 2944/2-1), and the European Commission under the PEGASOS project (grant no. 265148). T.
688 B. was supported by the Max Planck Graduate Center with the Johannes Gutenberg-
689 Universität Mainz (MPGC). The authors thank P. Spichtinger, U. K. Krieger, D. M. Lienhard,
690 B. P. Luo, T. Peter, A. T. Lambe, S. S. Steimer, D. A. Knopf and H.-P. Detté for stimulating
691 discussions.

692

693 **References**

694 Adler, G., Koop, T., Haspel, C., Taraniuk, I., Moise, T., Koren, I., Heiblum, R. H., and
695 Rudich, Y.: Formation of highly porous aerosol particles by atmospheric freeze-drying in ice
696 clouds, *Proc. Natl. Acad. Sci. USA*, 110, 20414-20419, 10.1073/pnas.1317209110, 2013.

697 Andreae, M. O., and Rosenfeld, D.: Aerosol-cloud-precipitation interactions. Part 1. The
698 nature and sources of cloud-active aerosols, *Earth Sci. Rev.*, 89, 13-41,
699 10.1016/j.earscirev.2008.03.001, 2008.

700 Angell, C. A.: in: *Relaxations in Complex Systems*, edited by: Ngai, K., and Wright, G. B.,
701 National Technical Information Service, I.S. Department of Commerce, Springfield, VA,
702 1985.

703 Angell, C. A.: Landscapes with megabasins: Polyamorphism in liquids and biopolymers and
704 the role of nucleation in folding and folding diseases, *Physica D*, 107, 122-142,
705 10.1016/s0167-2789(97)00077-8, 1997.

706 Baustian, K. J., Wise, M. E., Jensen, E. J., Schill, G. P., Freedman, M. A., and Tolbert, M. A.:
707 State transformations and ice nucleation in amorphous (semi-)solid organic aerosol, *Atmos.*
708 *Chem. Phys.*, 13, 5615-5628, 10.5194/acp-13-5615-2013, 2013.

709 Bones, D. L., Reid, J. P., Lienhard, D. M., and Krieger, U. K.: Comparing the mechanism of
710 water condensation and evaporation in glassy aerosol, *Proc. Natl. Acad. Sci. USA*, 109,
711 11613-11618, 10.1073/pnas.1200691109, 2012.

712 Claeys, M., Iinuma, Y., Szmigielski, R., Surratt, J. D., Blockhuys, F., Van Alsenoy, C., Boge,
713 O., Sierau, B., Gomez-Gonzalez, Y., Vermeylen, R., Van der Veken, P., Shahgholi, M., Chan,
714 A. W. H., Herrmann, H., Seinfeld, J. H., and Maenhaut, W.: Terpenylic Acid and Related

715 Compounds from the Oxidation of alpha-Pinene: Implications for New Particle Formation
716 and Growth above Forests, *Environ. Sci. Technol.*, 43, 6976-6982, 10.1021/es9007596, 2009.

717 Cziczo, D. J., Froyd, K. D., Hoose, C., Jensen, E. J., Diao, M. H., Zondlo, M. A., Smith, J. B.,
718 Twohy, C. H., and Murphy, D. M.: Clarifying the Dominant Sources and Mechanisms of
719 Cirrus Cloud Formation, *Science*, 340, 1320-1324, 10.1126/science.1234145, 2013.

720 DeMott, P. J., Cziczo, D. J., Prenni, A. J., Murphy, D. M., Kreidenweis, S. M., Thomson, D.
721 S., Borys, R., and Rogers, D. C.: Measurements of the concentration and composition of
722 nuclei for cirrus formation, *Proc. Natl. Acad. Sci. USA*, 100, 14655-14660,
723 10.1073/pnas.2532677100, 2003.

724 Dette, H. P., Qi, M. A., Schroder, D. C., Godt, A., and Koop, T.: Glass-Forming Properties of
725 3-Methylbutane-1,2,3-tricarboxylic Acid and Its Mixtures with Water and Pinonic Acid, *J.*
726 *Phys. Chem. A*, 118, 7024-7033, 10.1021/jp505910w, 2014.

727 Froyd, K. D., Murphy, D. M., Lawson, P., Baumgardner, D., and Herman, R. L.: Aerosols
728 that form subvisible cirrus at the tropical tropopause, *Atmos. Chem. Phys.*, 10, 209-218, 2010.

729 Fulcher, G. S.: Analysis of recent measurements of the viscosity of glasses, *J. Am. Ceram.*
730 *Soc.*, 8, 339-355, 10.1111/j.1151-2916.1925.tb16731.x, 1925.

731 Gunthe, S. S., King, S. M., Rose, D., Chen, Q., Roldin, P., Farmer, D. K., Jimenez, J. L.,
732 Artaxo, P., Andreae, M. O., Martin, S. T., and Pöschl, U.: Cloud condensation nuclei in
733 pristine tropical rainforest air of Amazonia: size-resolved measurements and modeling of
734 atmospheric aerosol composition and CCN activity, *Atmos. Chem. Phys.*, 9, 7551-7575,
735 10.5194/acp-9-7551-2009, 2009.

736 Hoose, C., and Möhler, O.: Heterogeneous ice nucleation on atmospheric aerosols: a review
737 of results from laboratory experiments, *Atmos. Chem. Phys.*, 12, 9817-9854, 10.5194/acp-12-
738 9817-2012, 2012.

739 Huisman, A. J., Krieger, U. K., Zuend, A., Marcolli, C., and Peter, T.: Vapor pressures of
740 substituted polycarboxylic acids are much lower than previously reported, *Atmos. Chem.*
741 *Phys.*, 13, 6647-6662, 10.5194/acp-13-6647-2013, 2013.

742 IPCC: Climate Change 2013, The Physical Science Basis, Cambridge University Press,
743 Cambridge, United Kingdom and New York, NY, USA, 2013.

744 Jain, A., Yang, G., and Yalkowsky, S. H.: Estimation of melting points of organic
745 compounds, *Ind. Eng. Chem. Res.*, 43, 7618-7621, 10.1021/ie049378m, 2004.

746 Jain, A., and Yalkowsky, S. H.: Estimation of melting points of organic compounds-II, *J.*
747 *Pharm. Sci.*, 95, 2562-2618, 10.1002/jps.20634, 2006.

748 Jensen, E. J., Smith, J. B., Pfister, L., Pittman, J. V., Weinstock, E. M., Sayres, D. S., Herman,
749 R. L., Troy, R. F., Rosenlof, K., Thompson, T. L., Fridlind, A. M., Hudson, P. K., Cziczo, D.
750 J., Heymsfield, A. J., Schmitt, C., and Wilson, J. C.: Ice supersaturations exceeding 100% at
751 the cold tropical tropopause: implications for cirrus formation and dehydration, *Atmos. Chem.*
752 *Phys.*, 5, 851-862, 2005.

753 Kalberer, M., Paulsen, D., Sax, M., Steinbacher, M., Dommen, J., Prevot, A. S. H., Fisseha,
754 R., Weingartner, E., Frankevich, V., Zenobi, R., and Baltensperger, U.: Identification of
755 polymers as major components of atmospheric organic aerosols, *Science*, 303, 1659-1662,
756 2004.

757 Kautzman, K. E., Surratt, J. D., Chan, M. N., Chan, A. W. H., Hersey, S. P., Chhabra, P. S.,
758 Dalleska, N. F., Wennberg, P. O., Flagan, R. C., and Seinfeld, J. H.: Chemical Composition of
759 Gas- and Aerosol-Phase Products from the Photooxidation of Naphthalene, *J. Phys. Chem. A*,
760 114, 913-934, 10.1021/jp908530s, 2010.

761 Kidd, C., Perraud, V., Wingen, L. M., and Finlayson-Pitts, B. J.: Integrating phase and
762 composition of secondary organic aerosol from the ozonolysis of α -pinene, *Proc. Natl. Acad.*
763 *Sci. USA*, 10.1073/pnas.1322558111, 2014.

764 Knopf, D. A., Wang, B., Laskin, A., Moffet, R. C., and Gilles, M. K.: Heterogeneous
765 nucleation of ice on anthropogenic organic particles collected in Mexico City, *Geophys. Res.*
766 *Letts.*, 37, L11803, 10.1029/2010gl043362, 2010.

767 Knopf, D. A., Alpert, P. A., Wang, B., O'Brien, R. E., Kelly, S. T., Laskin, A., Gilles, M. K.,
768 and Moffet, R. C.: Microspectroscopic imaging and characterization of individually identified
769 ice nucleating particles from a case field study, *J. Geophys. Res. Atmos.*, 119, JD021866,
770 2014.

771 Koop, T., Luo, B. P., Tsias, A., and Peter, T.: Water activity as the determinant for
772 homogeneous ice nucleation in aqueous solutions, *Nature*, 406, 611-614, 10.1038/35020537,
773 2000.

774 Koop, T., Bookhold, J., Shiraiwa, M., and Pöschl, U.: Glass transition and phase state of
775 organic compounds: dependency on molecular properties and implications for secondary
776 organic aerosols in the atmosphere, *Phys. Chem. Chem. Phys.*, 13, 19238-19255, 2011.

777 Kuwata, M., and Martin, S. T.: Phase of atmospheric secondary organic material affects its
778 reactivity, *Proc. Natl. Acad. Sci. USA*, 109, 17354-17359, 10.1073/pnas.1209071109, 2012.

779 Lambe, A. T., Onasch, T. B., Massoli, P., Croasdale, D. R., Wright, J. P., Ahern, A. T.,
780 Williams, L. R., Worsnop, D. R., Brune, W. H., and Davidovits, P.: Laboratory studies of the
781 chemical composition and cloud condensation nuclei (CCN) activity of secondary organic
782 aerosol (SOA) and oxidized primary organic aerosol (OPOA), *Atmos. Chem. Phys.*, 11, 8913-
783 8928, 10.5194/acp-11-8913-2011, 2011.

784 Lide, D. R.: *CRC Handbook of Chemistry and Physics*, CRC Press, National Institute of
785 Standards and Technology, Boca Raton, FL, 2005.

786 Lienhard, D. M., Bones, D. L., Zuend, A., Krieger, U. K., Reid, J. P., and Peter, T.:
787 Measurements of Thermodynamic and Optical Properties of Selected Aqueous Organic and
788 Organic-Inorganic Mixtures of Atmospheric Relevance, *J. Phys. Chem. A*, 116, 9954-9968,
789 10.1021/jp3055872, 2012.

790 Lienhard, D. M., Huisman, A. J., Bones, D. L., Te, Y. F., Luo, B. P., Krieger, U. K., and Reid,
791 J. P.: Retrieving the translational diffusion coefficient of water from experiments on single
792 levitated aerosol droplets, *Phys. Chem. Chem. Phys.*, 16, 16677-16683, 10.1039/c4cp01939c,
793 2014.

794 Marcolli, C.: Deposition nucleation viewed as homogeneous or immersion freezing in pores
795 and cavities, *Atmos. Chem. Phys.*, 14, 2071-2104, 10.5194/acp-14-2071-2014, 2014.

796 Mikhailov, E., Vlasenko, S., Martin, S. T., Koop, T., and Pöschl, U.: Amorphous and
797 crystalline aerosol particles interacting with water vapor: conceptual framework and
798 experimental evidence for restructuring, phase transitions and kinetic limitations, *Atmos.*
799 *Chem. Phys.*, 9, 9491-9522, 2009.

800 Murray, B. J., Wilson, T. W., Dobbie, S., Cui, Z. Q., Al-Jumur, S., Mohler, O., Schnaiter, M.,
801 Wagner, R., Benz, S., Niemand, M., Saathoff, H., Ebert, V., Wagner, S., and Karcher, B.:
802 Heterogeneous nucleation of ice particles on glassy aerosols under cirrus conditions, *Nature*
803 *Geosci.*, 3, 233-237, 10.1038/ngeo817, 2010.

804 O'Meara, S., Booth, A. M., Barley, M. H., Topping, D., and McFiggans, G.: An assessment of
805 vapour pressure estimation methods, *Phys. Chem. Chem. Phys.*, 16, 19453-19469,
806 10.1039/c4cp00857j, 2014.

807 Perraud, V., Bruns, E. A., Ezell, M. J., Johnson, S. N., Yu, Y., Alexander, M. L., Zelenyuk,
808 A., Imre, D., Chang, W. L., Dabdub, D., Pankow, J. F., and Finlayson-Pitts, B. J.:
809 Nonequilibrium atmospheric secondary organic aerosol formation and growth, *Proc. Natl.*
810 *Acad. Sci. USA*, 109, 2836-2841, 10.1073/pnas.1119909109, 2012.

811 Petters, M. D., and Kreidenweis, S. M.: A single parameter representation of hygroscopic
812 growth and cloud condensation nucleus activity, *Atmos. Chem. Phys.*, 7, 1961-1971, 2007.

813 Price, H. C., Murray, B. J., Mattsson, J., O'Sullivan, D., Wilson, T. W., Baustian, K. J., and
814 Benning, L. G.: Quantifying water diffusion in high-viscosity and glassy aqueous solutions
815 using a Raman isotope tracer method, *Atmos. Chem. Phys.*, 14, 3817-3830, 10.5194/acp-14-
816 3817-2014, 2014.

817 Pruppacher, H., and Klett, J.: *Microphysics of clouds and precipitation*, 2 ed., Kluwer
818 Academic Publishers, Boston, MA, 1997.

819 Rampp, M., Buttersack, C., and Ludemann, H. D.: c,T -dependence of the viscosity and the
820 self-diffusion coefficients in some aqueous carbohydrate solutions, *Carbohydr. Res.*, 328, 561-
821 572, 2000.

822 Renbaum-Wolff, L., Grayson, J. W., Bateman, A. P., Kuwata, K., Sellier, M., Murray, B. J.,
823 Schilling, J. E., Martin, S. T., and Bertram, A. K.: Viscosity of α -pinene secondary organic
824 material and implications for particle growth and reactivity, *Proc. Natl. Acad. Sci. USA*, 110,
825 8014-8019, 10.1073/pnas.1219548110 2013.

826 Rickards, A. M. J., Miles, R. E. H., Davies, J. F., Marshall, F. H., and Reid, J. P.:
827 Measurements of the Sensitivity of Aerosol Hygroscopicity and the kappa Parameter to the
828 O/C Ratio, *J. Phys. Chem. A*, 117, 14120-14131, 10.1021/jp407991n, 2013.

829 Saukko, E., Lambe, A. T., Massoli, P., Koop, T., Wright, J. P., Croasdale, D. R., Pedernera,
830 D. A., Onasch, T. B., Laaksonen, A., Davidovits, P., Worsnop, D. R., and Virtanen, A.:
831 Humidity-dependent phase state of SOA particles from biogenic and anthropogenic
832 precursors, *Atmos. Chem. Phys.*, 12, 7517-7529, 10.5194/acp-12-7517-2012, 2012.

833 Schill, G. P., and Tolbert, M. A.: Heterogeneous ice nucleation on phase-separated organic-
834 sulfate particles: effect of liquid vs. glassy coatings, *Atmos. Chem. Phys.*, 13, 4681-4695,
835 10.5194/acp-13-4681-2013, 2013.

836 Schill, G. P., De Haan, D. O., and Tolbert, M. A.: Heterogeneous Ice Nucleation on Simulated
837 Secondary Organic Aerosol, *Environ. Sci. Technol.*, 48, 1675-1682, 10.1021/es4046428,
838 2014.

839 Shilling, J. E., Chen, Q., King, S. M., Rosenoern, T., Kroll, J. H., Worsnop, D. R., DeCarlo,
840 P. F., Aiken, A. C., Sueper, D., Jimenez, J. L., and Martin, S. T.: Loading-dependent
841 elemental composition of alpha-pinene SOA particles, *Atmos. Chem. Phys.*, 9, 771-782,
842 2009.

843 Shiraiwa, M., Ammann, M., Koop, T., and Pöschl, U.: Gas uptake and chemical aging of
844 semisolid organic aerosol particles, *Proc. Natl. Acad. Sci. USA*, 108, 11003-11008,
845 10.1073/pnas.1103045108, 2011.

846 Shiraiwa, M., Pfrang, C., Koop, T., and Pöschl, U.: Kinetic multi-layer model of gas-particle
847 interactions in aerosols and clouds (KM-GAP): linking condensation, evaporation and
848 chemical reactions of organics, oxidants and water, *Atmos. Chem. Phys.*, 12, 2777-2794,
849 10.5194/acp-12-2777-2012, 2012.

850 Shiraiwa, M., Yee, L. D., Schilling, K. A., Loza, C. L., Craven, J. S., Zuend, A., Ziemann, P.
851 J., and Seinfeld, J. H.: Size distribution dynamics reveal particle-phase chemistry in organic
852 aerosol formation, *Proc. Natl. Acad. Sci. USA*, 110, 11746-11750, 10.1073/pnas.1307501110,
853 2013a.

854 Shiraiwa, M., Zuend, A., Bertram, A. K., and Seinfeld, J. H.: Gas-particle partitioning of
855 atmospheric aerosols: interplay of physical state, non-ideal mixing and morphology, *Phys.
856 Chem. Chem. Phys.*, 15, 11441-11453, 10.1039/C3CP51595H, 2013b.

857 Song, M., Marcolli, C., Krieger, U. K., Zuend, A., and Peter, T.: Liquid-liquid phase
858 separation and morphology of internally mixed dicarboxylic acids/ammonium sulfate/water
859 particles, *Atmos. Chem. Phys.*, 12, 2691-2712, 10.5194/acp-12-2691-2012, 2012.

860 Surratt, J. D., Murphy, S. M., Kroll, J. H., Ng, N. L., Hildebrandt, L., Sorooshian, A.,
861 Szmigielski, R., Vermeylen, R., Maenhaut, W., Claeys, M., Flagan, R. C., and Seinfeld, J. H.:
862 Chemical composition of secondary organic aerosol formed from the photooxidation of
863 isoprene, *J. Phys. Chem. A*, 110, 9665-9690, 10.1021/jp061734m, 2006.

864 Szmigielski, R., Surratt, J. D., Gomez-Gonzalez, Y., Van der Veken, P., Kourtchev, I.,
865 Vermeylen, R., Blockhuys, F., Jaoui, M., Kleindienst, T. E., Lewandowski, M., Offenberg, J.
866 H., Edney, E. O., Seinfeld, J. H., Maenhaut, W., and Claeys, M.: 3-methyl-1,2,3-
867 butanetricarboxylic acid: An atmospheric tracer for terpene secondary organic aerosol,
868 *Geophys. Res. Lett.*, 34, 6, 10.1029/2007gl031338, 2007.

869 Tammann, G., and Hesse, W.: The dependency of viscosity on temperature in hypothermic
870 liquids, *Z. Anorg. Allg. Chem.*, 156, 14, 1926.

871 Tong, H. J., Reid, J. P., Bones, D. L., Luo, B. P., and Krieger, U. K.: Measurements of the
872 timescales for the mass transfer of water in glassy aerosol at low relative humidity and
873 ambient temperature, *Atmos. Chem. Phys.*, 11, 4739-4754, 10.5194/acp-11-4739-2011, 2011.

874 Vaden, T. D., Imre, D., Beranek, J., Shrivastava, M., and Zelenyuk, A.: Evaporation kinetics
875 and phase of laboratory and ambient secondary organic aerosol, *Proc. Natl. Acad. Sci. USA*,
876 108, 2190-2195, 10.1073/pnas.1013391108, 2011.

877 Virtanen, A., Joutsensaari, J., Koop, T., Kannosto, J., YliPirilä, P., Leskinen, J., Mäkelä, J.
878 M., Holopainen, J. K., Pöschl, U., Kulmala, M., Worsnop, D. R., and Laaksonen, A.: An
879 amorphous solid state of biogenic secondary organic aerosol particles, *Nature*, 467, 824-827,
880 doi:10.1038/nature09455, 2010.

881 Vogel, H.: The temperature dependence law of the viscosity of fluids, *Physik. Z.*, 22, 645-
882 646, 1921.

883 Wagner, R., Mohler, O., Saathoff, H., Schnaiter, M., Skrotzki, J., Leisner, T., Wilson, T. W.,
884 Malkin, T. L., and Murray, B. J.: Ice cloud processing of ultra-viscous/glassy aerosol particles
885 leads to enhanced ice nucleation ability, *Atmos. Chem. Phys.*, 12, 8589-8610, 10.5194/acp-
886 12-8589-2012, 2012.

887 Wang, B. B., Lambe, A. T., Massoli, P., Onasch, T. B., Davidovits, P., Worsnop, D. R., and
888 Knopf, D. A.: The deposition ice nucleation and immersion freezing potential of amorphous
889 secondary organic aerosol: Pathways for ice and mixed-phase cloud formation, *J. Geophys.*
890 *Res. Atmos.*, 117, D16209, 10.1029/2012jd018063, 2012.

891 Wilson, T. W., Murray, B. J., Wagner, R., Mohler, O., Saathoff, H., Schnaiter, M., Skrotzki,
892 J., Price, H. C., Malkin, T. L., Dobbie, S., and Al-Jumur, S.: Glassy aerosols with a range of
893 compositions nucleate ice heterogeneously at cirrus temperatures, *Atmos. Chem. Phys.*, 12,
894 8611-8632, 10.5194/acp-12-8611-2012, 2012.

895 Yee, L. D., Craven, J. S., Loza, C. L., Schilling, K. A., Ng, N. L., Canagaratna, M. R.,
896 Ziemann, P. J., Flagan, R. C., and Seinfeld, J. H.: Secondary organic aerosol formation from
897 low-NO_x photooxidation of dodecane: evolution of multigeneration gas-phase chemistry and
898 aerosol composition, *J. Phys. Chem. A*, 116, 6211-6230, 2012.

899 You, Y., Renbaum-Wolff, L., Carreras-Sospedra, M., Hanna, S. J., Hiranuma, N., Kamal, S.,
900 Smith, M. L., Zhang, X. L., Weber, R. J., Shilling, J. E., Dabdub, D., Martin, S. T., and
901 Bertram, A. K.: Images reveal that atmospheric particles can undergo liquid-liquid phase
902 separations, *Proc. Natl. Acad. Sci. USA*, 109, 13188-13193, 10.1073/pnas.1206414109, 2012.

903 You, Y., Smith, M. L., Song, M. J., Martin, S. T., and Bertram, A. K.: Liquid-liquid phase
904 separation in atmospherically relevant particles consisting of organic species and inorganic
905 salts, *International Reviews in Physical Chemistry*, 33, 43-77,
906 10.1080/0144235x.2014.890786, 2014.

907 Yu, H., Kaufman, Y. J., Chin, M., Feingold, G., Remer, L. A., Anderson, T. L., Balkanski, Y.,
908 Bellouin, N., Boucher, O., Christopher, S., DeCola, P., Kahn, R., Koch, D., Loeb, N., Reddy,
909 M. S., Schulz, M., Takemura, T., and Zhou, M.: A review of measurement-based assessments
910 of the aerosol direct radiative effect and forcing, *Atmos. Chem. Phys.*, 6, 613-666, 2006.

911 Zhang, X., Schwantes, R. H., Coggon, M. M., Loza, C. L., Schilling, K. A., Flagan, R. C., and
912 Seinfeld, J. H.: Role of ozone in SOA formation from alkane photooxidation, *Atmos. Chem.*
913 *Phys.*, 14, 1733-1753, 10.5194/acp-14-1733-2014, 2014.

914 Zhou, S., Shiraiwa, M., McWhinney, R., Pöschl, U., and Abbatt, J. P. D.: Kinetic limitations
915 in gas-particle reactions arising from slow diffusion in secondary organic aerosol, *Faraday*
916 *Discuss.*, 165, 391-406, 10.1039/C3FD00030C, 2013.

917 Zobrist, B., Weers, U., and Koop, T.: Ice nucleation in aqueous solutions of poly ethylene
918 glycol with different molar mass, *J. Chem. Phys.*, 118, 10254-10261, 10.1063/1.1571818,
919 2003.

920 Zobrist, B., Marcolli, C., Pedernera, D. A., and Koop, T.: Do atmospheric aerosols form
921 glasses?, *Atmos. Chem. Phys.*, 8, 5221-5244, 2008.

922 Zobrist, B., Soonsin, V., Luo, B. P., Krieger, U. K., Marcolli, C., Peter, T., and Koop, T.:
923 Ultra-slow water diffusion in aqueous sucrose glasses, *Phys. Chem. Chem. Phys.*, 13, 3514-
924 3526, 10.1039/c0cp01273d, 2011.

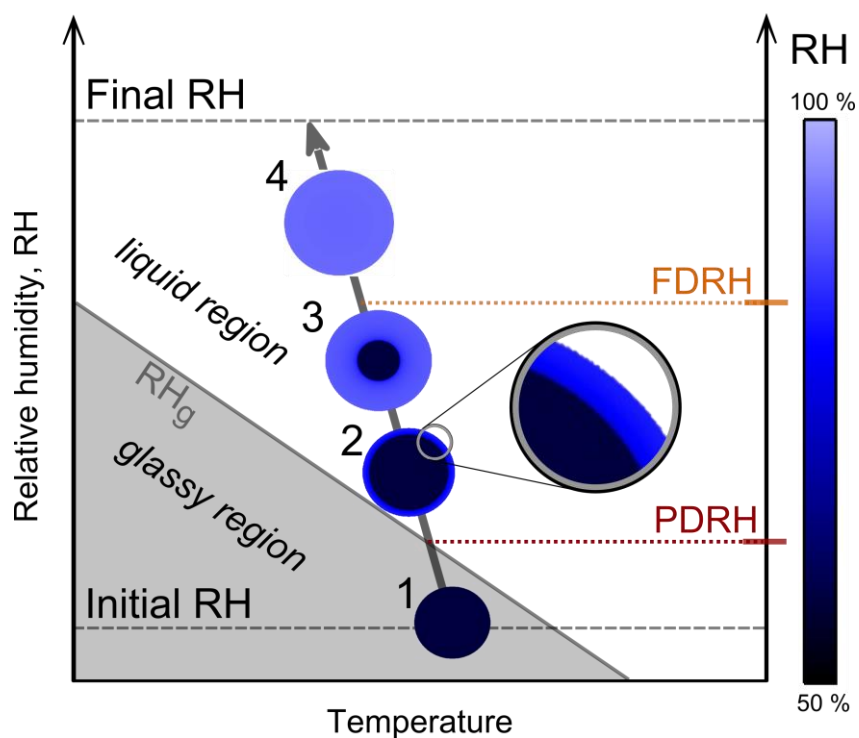
925 Zuend, A., and Seinfeld, J. H.: Modeling the gas-particle partitioning of secondary organic
926 aerosol: the importance of liquid-liquid phase separation, *Atmos. Chem. Phys.*, 12, 3857-
927 3882, 10.5194/acp-12-3857-2012, 2012.

928

929 Table A1. Assumed physical properties of SOA classes for use in conjunction with diffusivity
 930 estimation scheme.

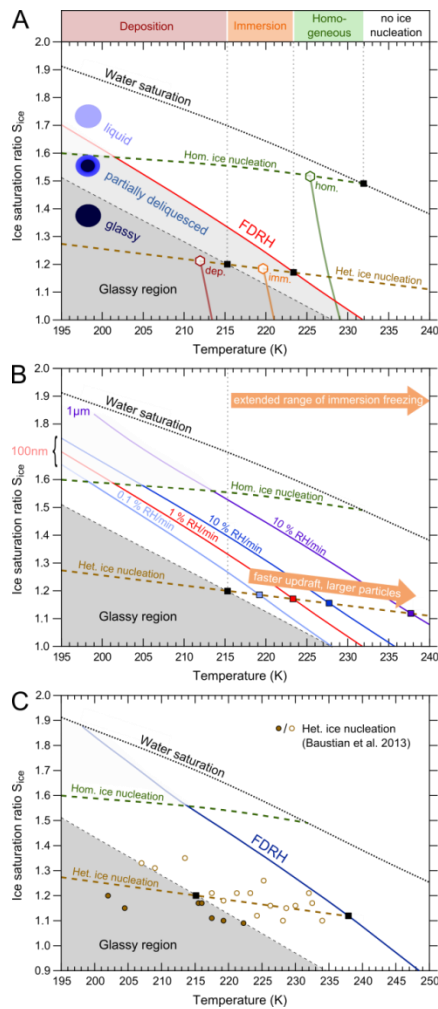
SOA Class	O/C	$T_{g,org}$ (K)	k_{GT}	κ_{org}
A-PINENE	0.3	228.9 ± 10.6	2.5	0.084 ± 0.012
	0.5	278.5 ± 7.0	2.5	0.120 ± 0.020
	0.7	328.1 ± 12.8	2.5	0.156 ± 0.028
ISOPRENE	0.6	258.2 ± 22.2	2.5	0.138 ± 0.024
	0.8	287.2 ± 11.9	2.5	0.174 ± 0.032
	1.0	316.3 ± 19.1	2.5	0.210 ± 0.040
NAPHTHALENE	0.3	294.2 ± 5.7	2.5	0.084 ± 0.012
	0.5	313.1 ± 8.8	2.5	0.120 ± 0.020
	0.7	332.0 ± 15.0	2.5	0.156 ± 0.028
DODECANE	0.1	210.3 ± 9.7	2.5	0.048 ± 0.004
	0.3	216.8 ± 5.1	2.5	0.084 ± 0.012
	0.5	223.4 ± 11.4	2.5	0.120 ± 0.020
KOOP SOA	---	270 ± 21	2.5 ± 1	$0.1008^{+0.1008}$ -0.0504

931



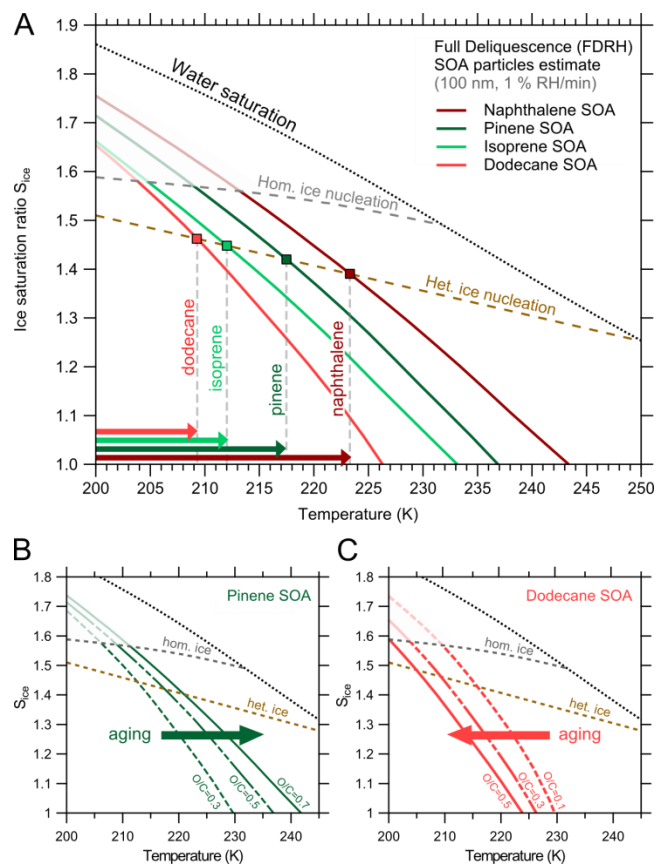
932

933 Figure 1. Schematic temporal evolution of particle morphology along a trajectory of an
 934 atmospheric updraft (grey arrow). Humidification of ambient air upon adiabatic expansion
 935 leads to liquefaction of initially glassy particles (dark blue color, 1) via core-shell
 936 morphologies (2, 3) to liquid particles (light blue color, 4). Whereas partial deliquescence
 937 (PDRH) coincides with RH_g , full deliquescence (FDRH) is delayed to much higher RH,
 938 indicating that diffusion processes occur on much longer time scales than humidification. The
 939 speed of the displayed trajectory corresponds to that typical for cloud chamber or
 940 environmental cell experiments ($0.1 - 1.5 \text{ K min}^{-1}$, $1 - 15 \text{ \% RH min}^{-1}$).



941

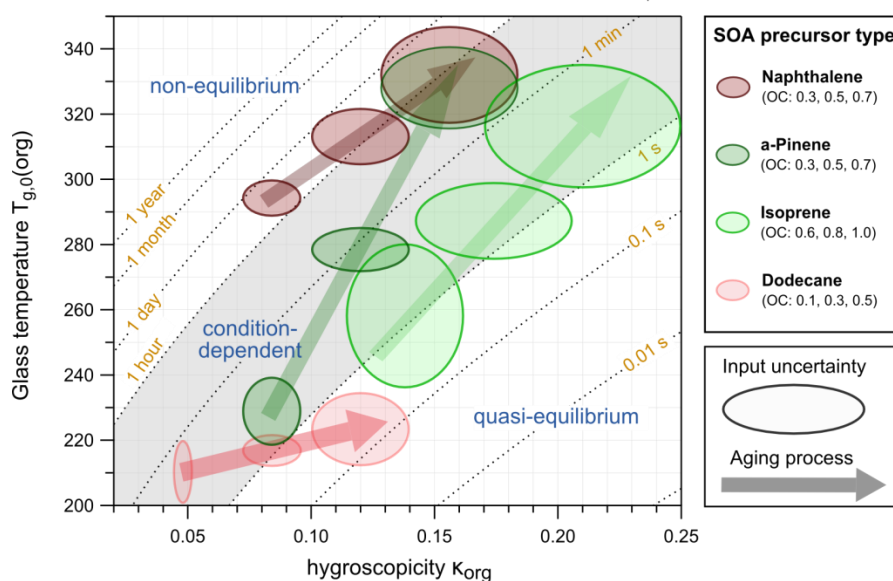
942 Figure 2. (A) Simulated regimes of heterogeneous and homogeneous ice nucleation in the
 943 humidification of sucrose particles. The red solid line indicates full deliquescence relative
 944 humidities (FDRH) for 100 nm particles exposed to a humidification rate of 1 % RH min⁻¹ (\approx
 945 0.2 m s⁻¹ atmospheric updraft). Example trajectories start at ice saturation, follow a constant
 946 dew point line and end at expected ice nucleation (hexagonal markers) with deposition (red),
 947 immersion (orange), and homogeneous (green) freezing. (B) Effects of different particles
 948 sizes and humidification rates on FDRH. The upper boundary for immersion freezing is
 949 extended to high temperatures for large particle radii and high humidification rates and is
 950 expected to occur up to 238 K for the most extreme scenario (1 μm , 10 % RH min⁻¹, purple
 951 solid line). (C) Application to the experimental conditions in Baustian et al. (2013), i.e. 4 μm
 952 particles humidified at a rate of 1 % RH min⁻¹, leads to FDRH that is able to explain all
 953 observed experimental ice onsets (brown circles). The thermodynamic glass transition divides
 954 the experimental data in events of deposition ice nucleation (closed circles) and immersion
 955 freezing (open circles).



956

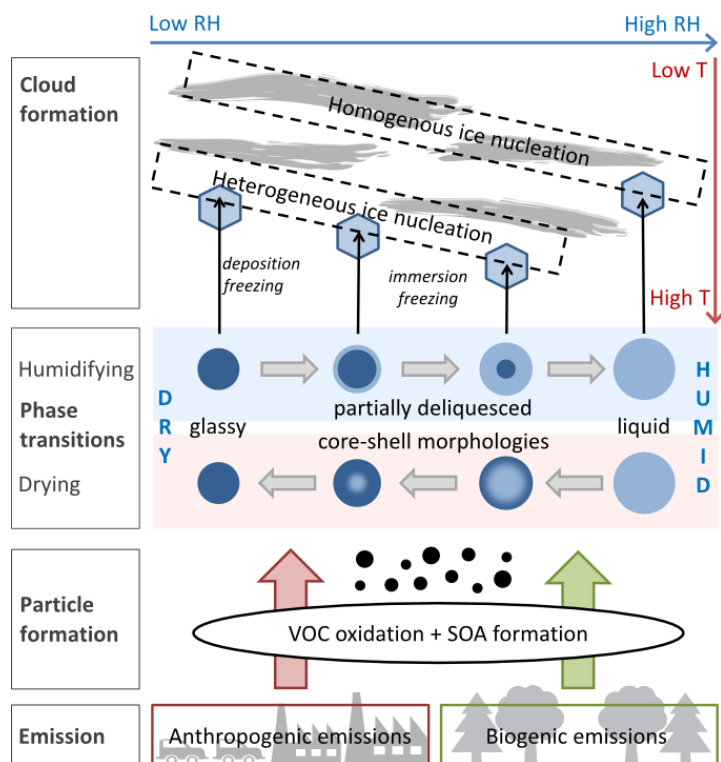
957 Figure 3. (A) Simulated humidification of SOA particles from the four different precursors a-
 958 pinene, isoprene, dodecane and naphthalene. Naphthalene SOA (dark red) shows the latest
 959 deliquescence, whereas dodecane SOA (light red) liquefied rather early in the simulations.
 960 The two biogenic SOA estimates lie between both extremes with pinene SOA (dark green)
 961 showing slightly later deliquescence than isoprene SOA. Intercepts (square markers) with a
 962 heterogeneous nucleation onset typical for SOA (brown dashed line) indicate upper
 963 temperature limits for immersion freezing (arrows on x-axis). The effect of particle ageing
 964 also depends on precursor type: Pinene SOA (B) shows hardening upon increase in O/C
 965 (indicated by higher FDRH), whereas dodecane SOA (C) exhibits softening (indicated by
 966 lower FDRH). Similarly, isoprene and naphthalene SOA show only moderate hardening and
 967 softening, respectively (Fig. S5).

Water diffusion time scales in SOA (220 K, $S_{ice} = 1.45$, $d_p = 100$ nm)

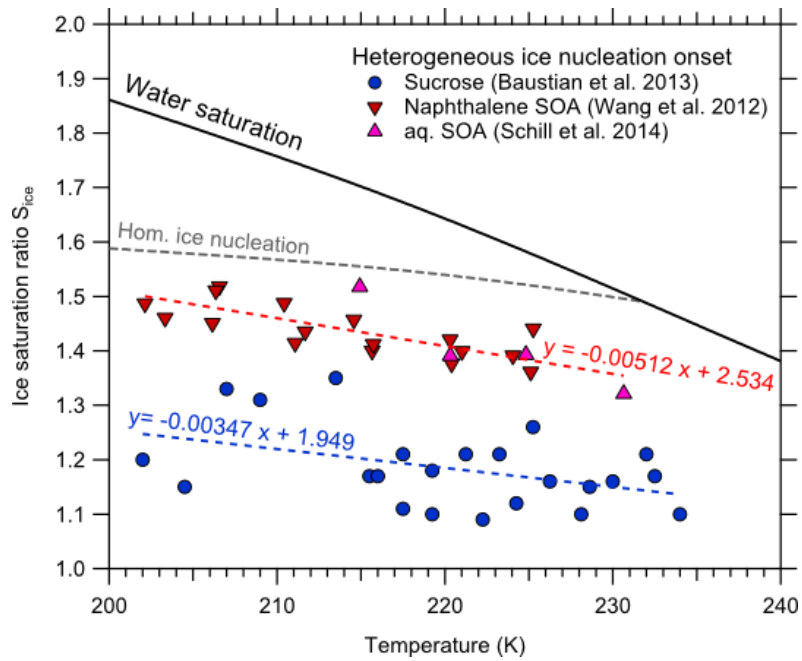


968

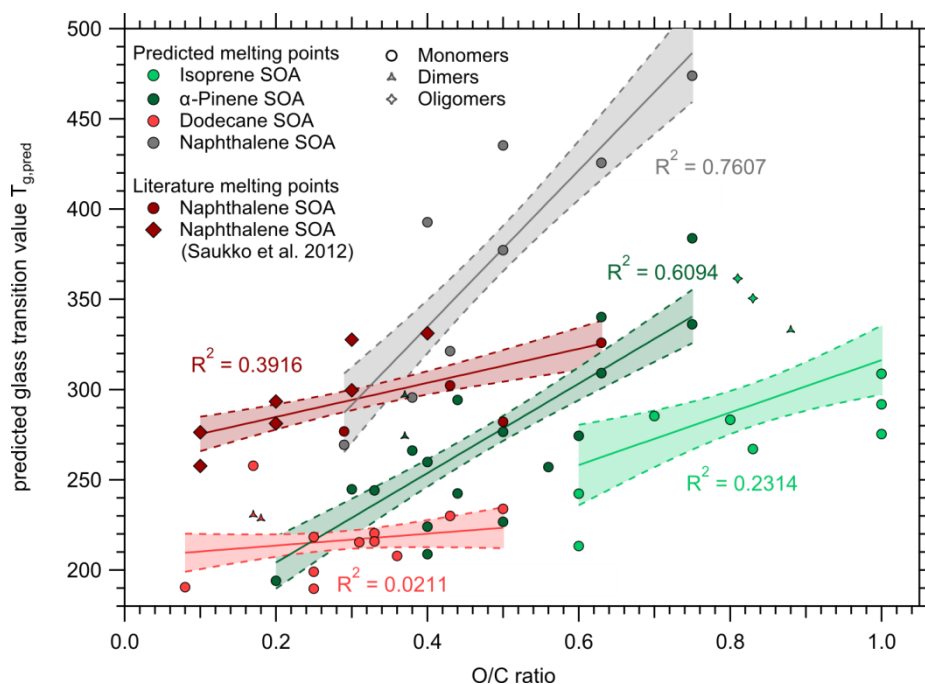
969 Figure 4. Characteristic time scales of water diffusion in SOA as function of hygroscopicity
 970 κ_{org} and glass transition temperatures of the pure organic matrix $T_{g,org}$. Calculations have been
 971 performed at 220 K, $S_{ice} = 1.45$ and for 100 nm particles. Oval shapes confine estimated
 972 ranges in κ_{org} and $T_{g,org}$ for the four SOA types in three different oxidation states (Appendix A
 973 and Table A1). The grey area indicates the time scale of typical atmospheric updrafts (1 s to 1
 974 h) and thus divides the plot in areas of quasi-equilibrium and non-equilibrium water diffusion.
 975 Within the grey area, the relative speed of both processes depends upon the actual
 976 atmospheric conditions. The aging process is indicated by arrows pointing from regions of
 977 low O/C to regions of high O/C.



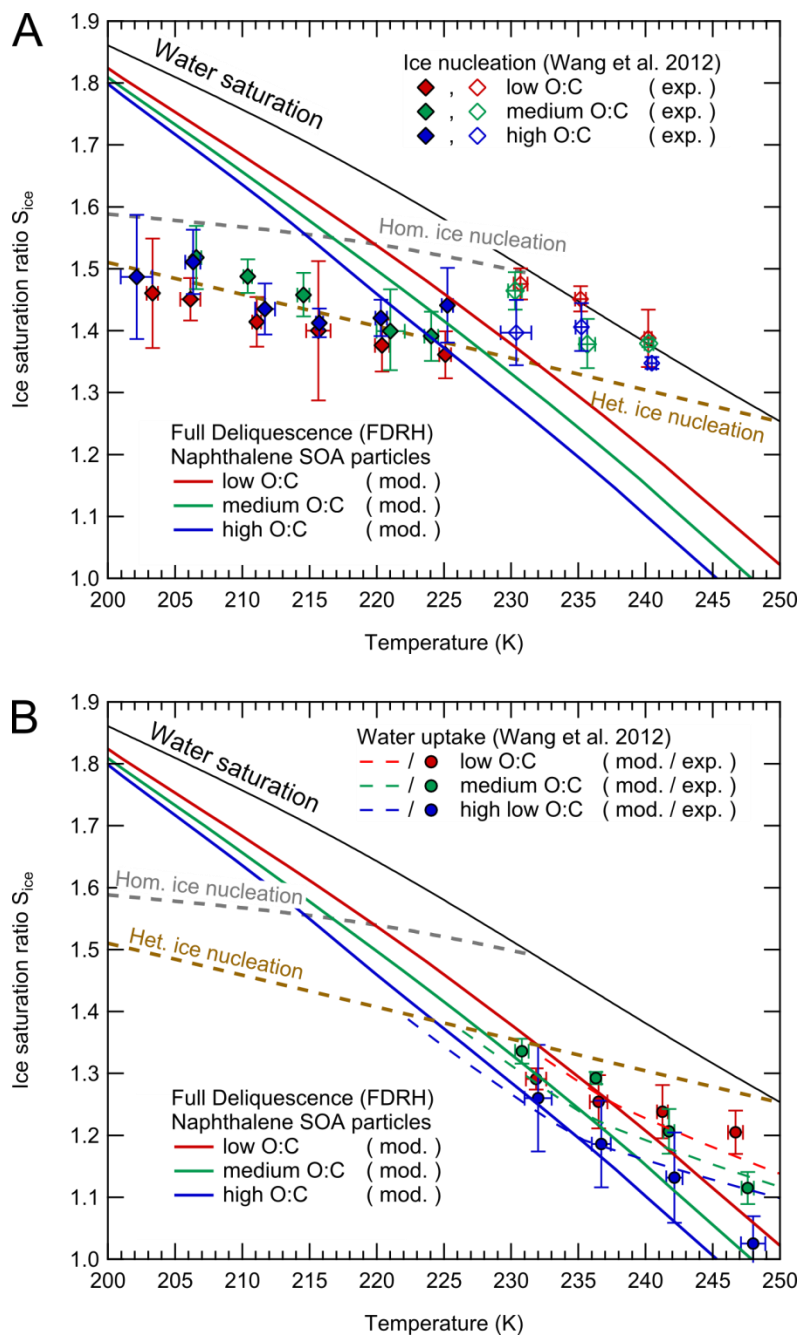
1
 2 Figure 5. Overview of processes in organic aerosol particles affecting atmospheric cloud
 3 formation. Particles form by oxidation of volatile organic compounds (VOCs) originating
 4 from anthropogenic and biogenic emissions. The dominating cloud formation process
 5 depends on particle phase state, which is a function of temperature and humidity. Humidity-
 6 induced phase transitions between phase states may be kinetically limited and occur under
 7 formation of partially deliquesced particles with core-shell morphologies. Glassy or partially
 8 deliquesced particles are able to undergo heterogeneous ice nucleation, occurring at lower
 9 relative humidity or higher temperature than homogeneous ice nucleation of liquid particles.



1
 2 Figure A1. Determination of heterogeneous ice nucleation onsets. For sucrose, data from
 3 Baustian et al. (2013) (blue circles) are fitted. For SOA, deposition freezing data on
 4 Naphthalene SOA from Wang et al. (2012) (red downward triangles) as well as nucleation
 5 data on aqSOA from Schill et al. (2014) (pink upward triangles) are used. The resulting linear
 6 regression fits (blue and red dashed lines) lie significantly below the homogeneous nucleation
 7 limit and are displayed along with their parameterizations.

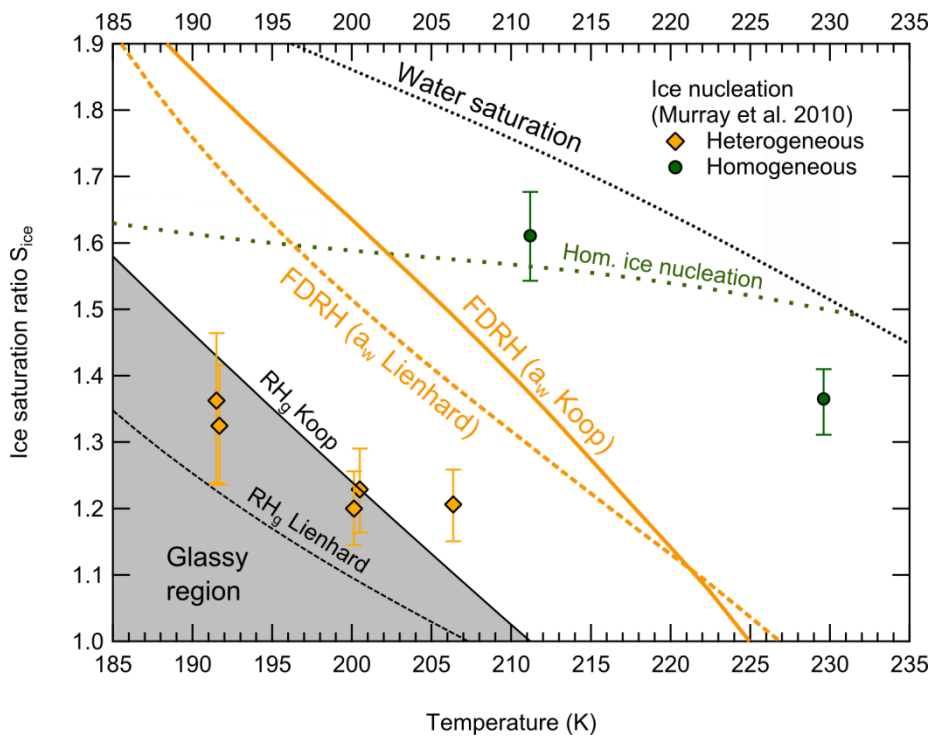


1
 2 Figure A2. Predicted glass transition values of SOA marker substances as function of O/C
 3 ratio. The predicted $T_{g,org}$ exhibit a linear correlation with O/C for each of the four SOA
 4 systems. Solid lines are robust linear regressions using a bisquare weighting function and
 5 shaded areas are confidence intervals at the 1σ level. Anthropogenic aliphatic SOA
 6 constituents show the lowest values of $T_{g,org}$ and a weak dependence on O/C. In contrast,
 7 aromatic SOA shows the highest glass transition values despite a rather low average O/C
 8 ratio.



1

2 Figure B1. Comparison between calculation results of naphthalene SOA deliquescence and
 3 experimental ice nucleation and water uptake data from Wang et al. (2012). For the numerical
 4 simulations, aerosol particles are assumed to be 1 μm in diameter and are humidified at a rate
 5 of 1 % RH min^{-1} , corresponding to a cooling rate of about 0.1 K min^{-1} used by Wang et al.



1

2 Figure B2. Comparison between calculation results of citric acid aerosol deliquescence
 3 (orange lines) and experimental ice nucleation data from Murray et al. (2010) (orange
 4 diamonds, green circles). In the numerical simulations, 150 nm diameter aerosol particles are
 5 humidified at a rate of 12 % RH min⁻¹, corresponding to a cooling rate around 1-2 K min⁻¹
 6 typical for cloud chamber experiments. Black lines and shaded areas confine the region where
 7 a glass is the favored thermodynamic state. The dashed lines were obtained using the water
 8 activity parameterization provided by Lienhard et al. (2012), whereas the solid lines were
 9 obtained with the parameterization in Koop et al. (2011).